

Complex-Valued Holographic Radiance Fields

YICHENG ZHAN, University College London, United Kingdom

DONG-HA SHIN, Pohang University of Science and Technology (POSTECH), South Korea

SEUNG-HWAN BAEK, Pohang University of Science and Technology (POSTECH), South Korea

KAAN AKŞIT, University College London, United Kingdom

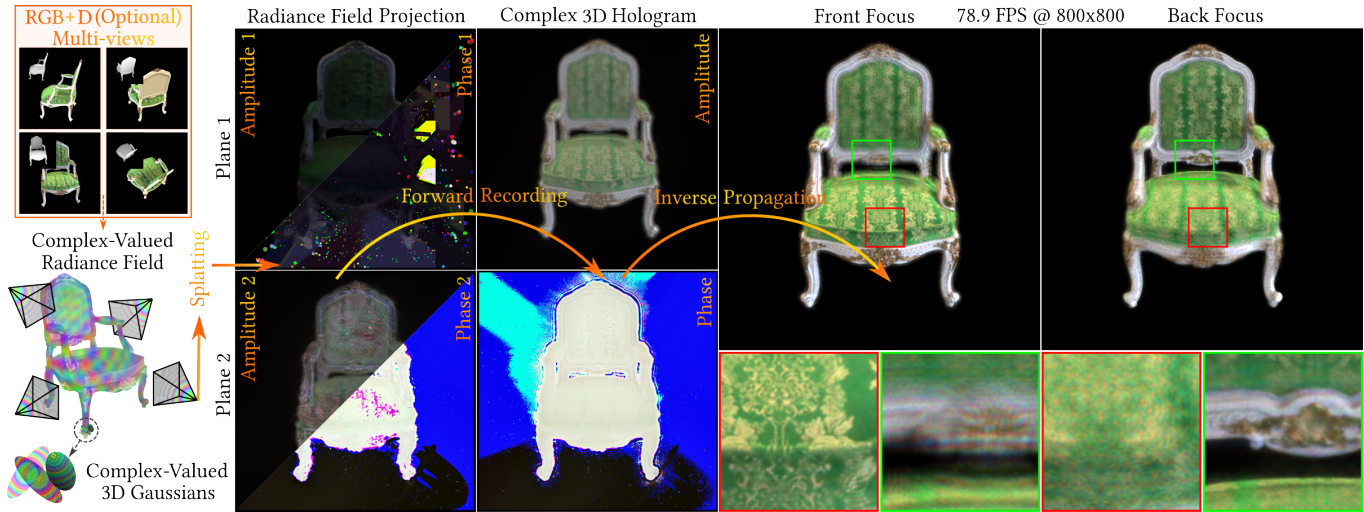


Fig. 1. Complex-Valued Holographic Radiance Fields. Instead of considering interference and diffraction as a secondary derivation from intensity data, our method explicitly treats the complex-valued holographic radiance fields as the primary optimization variable at the beginning of the scene modeling, jointly optimizing the 3D scene across multiple viewpoints to model intensity, interference, and diffraction of light in scene representation. The complex-valued 3D Gaussians will be projected to multiple depth planes, resulting in a complex 3D hologram via holographic rendering. This enables holographic reconstruction with depth-of-field effects: green boxes highlight the back focus region, and red boxes show the front focus region.

Modeling the full properties of light, including both amplitude and phase, in 3D representations is crucial for advancing physically plausible rendering, particularly in holographic displays. To support these features, we propose a novel representation that optimizes 3D scenes without relying on intensity-based intermediaries. We reformulate 3D Gaussian splatting with complex-valued Gaussian primitives, expanding support for rendering with light waves. By leveraging RGBD multi-view images, our method directly optimizes complex-valued Gaussians as a 3D holographic scene representation. This eliminates the need for computationally expensive hologram re-optimization. Compared with state-of-the-art methods, our method achieves 30x-10,000x speed improvements while maintaining on-par image

quality, representing a first step towards geometrically aligned, physically plausible holographic scene representations.

CCS Concepts: • **Computing methodologies** → **Mixed / augmented reality**; **3D imaging**; **Computer graphics**; **Rendering**.

Additional Key Words and Phrases: Novel View Synthesis, Radiance Fields, 3D Gaussians, Computer-Generated Holography

ACM Reference Format:

Yicheng Zhan, Dong-Ha Shin, Seung-Hwan Baek, and Kaan Akşit. 2024. Complex-Valued Holographic Radiance Fields. 1, 1 (June 2024), 28 pages. <https://doi.org/XXXXXXX.XXXXXXX>

1 Introduction

Light exhibits numerous physical phenomena beyond intensity, such as spectral variation, polarization, diffraction, and interference [Goodman 2005]. Recent advancements in 3D Gaussian Splatting (3DGS) [Kerbl et al. 2023] have enabled efficient novel-view synthesis for geometry-aware 3D scene representation. However, these approaches focus solely on intensity-based modeling and thus neglect the wave-optics properties introduced above. Modeling these wave-optics properties accurately is essential for physically plausible rendering of visual scenes. Among these properties, diffraction and interference are fundamental to holographic displays. Unlike conventional displays, holographic displays are an emerging technology that creates immersive 3D experiences. By

Authors' addresses: Yicheng Zhan, UCABY83@ucl.ac.uk, University College London, Gower Street, London, United Kingdom, WC1E 6BT; Dong-Ha Shin, 0218sdh@gmail.com, Pohang University of Science and Technology (POSTECH), 77 Cheongam-ro, Nam-gu, Pohang-si, South Korea, 37673; Seung-Hwan Baek, shwbaek@postech.ac.kr, Pohang University of Science and Technology (POSTECH), 77 Cheongam-ro, Nam-gu, Pohang-si, South Korea, 37673; Kaan Akşit, University College London, Gower Street, London, United Kingdom, k.aksit@ucl.ac.uk.

Permission to make digital or hard copies of all or part of this work for personal or classroom use is granted without fee provided that copies are not made or distributed for profit or commercial advantage and that copies bear this notice and the full citation on the first page. Copyrights for components of this work owned by others than ACM must be honored. Abstracting with credit is permitted. To copy otherwise, or republish, to post on servers or to redistribute to lists, requires prior specific permission and/or a fee. Request permissions from permissions@acm.org.

© 2024 Association for Computing Machinery.

XXXX-XXXX/2024/6-ART \$15.00

<https://doi.org/XXXXXXX.XXXXXXX>

reconstructing light diffraction—in other words, the phase from a hologram—holographic displays can reproduce the depth cues that our visual system perceives in natural environments [Kim et al. 2024].

Computer-Generated Holography (CGH) is the computational backbone of holographic displays, enabling the synthesis of holograms that reconstruct 3D wavefronts. Existing CGH methods decouple phase retrieval from scene representation, treating hologram synthesis as a post-processing step applied after the intensity distribution is determined. These methods typically estimate phase patterns that reproduce desired reconstructed intensity image for a fixed perspective [Chakravarthula et al. 2020; Choi et al. 2025, 2021a; Hossein Eybposh et al. 2020; Kavaklı et al. 2023a,b; Liu et al. 2023; Peng et al. 2020; Schiffers et al. 2023; Shi et al. 2021, 2022] and a narrow viewing angles [Chakravarthula et al. 2022; Chao et al. 2024; Chen et al. 2025; Kim et al. 2024; Wang et al. 2024]. This viewpoint-specific wave propagation requires recalculating diffraction patterns when the geometric relationship between the object and hologram plane changes. In this context, phase values function as computational variables optimized for specific views, not as intrinsic properties of the 3D scene. As shown in Fig. 2, the estimated phase fails to align with the scene geometry across novel views, leading to visual artifacts during geometric transitions and physically inconsistent wave optics effects. Existing CGH methods [Choi et al. 2025; Kavaklı et al. 2023b; Shi et al. 2022] typically require view-dependent transformations or complete recalculation of holograms for each viewpoint to maintain consistency.

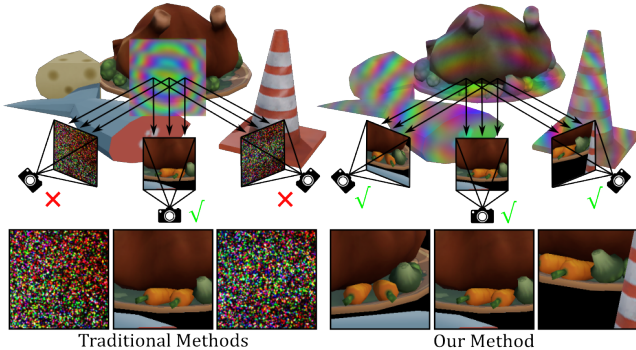


Fig. 2. Left: Traditional CGH methods calculate hologram for a single view, but the wavefront collapses when the geometric configuration changes, requiring recalculation for each viewpoint. Right: A complex-valued holographic radiance field stores a scene-wide, geometrically aligned phase; the rainbow bands depict geometry-aligned phase.

Our work aims to coherently merge traditional intensity-based radiance fields and holography. We present a novel framework that extends 3DGS by using complex-valued Gaussian primitives to model both amplitude and phase information of the scene. Our method explicitly treats the complex-valued holographic radiance field as the primary optimization target at the beginning of scene modeling, without the need for per-view transformation. We jointly optimize the scene across multiple viewpoints to model interference and diffraction phenomena directly. We propose a differentiable rasterizer that effectively renders complex-valued Gaussian primitives

using learnable probabilistic assignments. Unlike existing Eulerian-based CGH methods that require per-primitive calculations scaling quadratically with the number of primitives, our Lagrangian-based approach is more effective due to the linear relationship between the number of primitives and complexity, achieving 30x-10,000x speed improvements over state-of-the-art methods [Choi et al. 2025]. By optimizing directly in the complex domain across multiple views, our method achieves geometrically aligned, view-dependent diffraction and interference effects without relying on intensity-based intermediaries, representing a first step towards physically plausible holographic scene representations. Specifically, our contributions include:

- We present complex-valued holographic radiance fields, a Lagrangian-based complex-valued Gaussian representation for transformation-free, geometrically aligned holographic rendering.
- We propose a novel differentiable rasterizer, enabling efficient rendering and optimization of complex-valued holographic radiance fields.

2 Related Work

Our approach bridges recent advances in neural rendering with holography, enabling the efficient generation of holograms from novel views. We will first review novel-view synthesis and then examine existing wave optics rendering techniques that also attempt to simulate light phenomena beyond intensity. Finally, we discuss the traditional CGH methods in general, including point-based, polygon-based, and layer-based CGH methods.

2.1 Novel-View Synthesis

Traditional novel-view synthesis methods focus exclusively on modeling intensity and appearance, which limits their applicability to emerging display technologies that require holographic properties. Early image-based rendering approaches [Chaurasia et al. 2013] and volumetric methods [Hedman et al. 2017; Riegler and Koltun 2020] established the foundation for view-dependent appearance modeling. The introduction of Neural Radiance Fields (NeRF) [Mildenhall et al. 2021] changed the field by learning continuous radiance functions that encode view-dependent color and opacity. Subsequent extensions improved quality and efficiency [Barron et al. 2021, 2022, 2023; Chen et al. 2022; Duckworth et al. 2024; Niemeyer et al. 2024; Rebaín et al. 2021].

Point-based representations have recently advanced with 3DGS [Kerbl et al. 2023], emerging as a promising alternative to NeRF. 3DGS offers a promising foundation for our work, as it encodes both geometry and appearance using oriented Gaussian primitives. Unlike implicit representations, 3DGS provides explicit geometric primitives that naturally align with holographic modeling principles, but it is fundamentally limited to intensity-based representations. Our work extends 3DGS to include intrinsic amplitude and phase properties, enabling the modeling of complex-valued holographic radiance fields that capture not just intensity, but also the interference and diffraction phenomena.

Rendering Beyond Intensity. The work by Kim et al. [2023] extends NeRF beyond intensity-based representations to capture spectral and polarimetric properties of light, revealing richer material and structural characteristics of 3D scenes. Notably, spectral and polarization data can be supervised using ground-truth measurements obtained from specialized imaging devices. On the other hand, interference and diffraction phenomena arise from the accumulation of phase and amplitude values. Interference and diffraction effects lack direct measurement data and must be inferred through computational means, as holographic cameras capable of capturing both amplitude and phase information are not yet commodity equipment [An et al. 2020]. Moreover, supporting simulations of holography in rendering pipelines is a common theme in research. For instance, Steinberg et al. [2024; 2022] introduced wave optics formulations for path tracing, enabling partial coherence and diffraction effects. Choi et al. [2025] proposed Gaussian Wave Splatting (GWS) that transforms 2D Gaussian scenes into holograms by deriving closed-form solutions for angular spectrum. Chen et al. [2025] proposed a two-stage method that combines pretrained intensity-based 3DGS with U-Net [Ronneberger et al. 2015], enabling efficient hologram synthesis for novel views.

2.2 Eulerian-based Computer-Generated Holography

Holographic displays rely on CGH, which algorithmically synthesizes diffraction and interference patterns to reconstruct 3D scenes with near-accurate depth cues. Conceptually, traditional CGH methods follow a per-view Eulerian approach to wave propagation, where the coordinates on the hologram plane remain fixed, while the complex field varies when the relationship between the scene geometry and the viewpoint changes, requiring recalculation. The computed holographic patterns are implemented by Spatial Light Modulator (SLM), which modulates the phase and optionally amplitude of incident coherent beams to generate designed interference fringes. Through numerical wave propagation simulations [Kavaklı et al. 2022; Peng et al. 2020], CGH generates holograms leading to high spatio-angular resolution, as an emerging screen technology. The accuracy and computational complexity of CGH strongly depend on primitive representations, generally categorized into point-based, polygon-based, and layer-based methods.

Point-based CGH represents scenes using discrete points emitting spherical waves. The wave field at the hologram, P , is calculated by summing waves from N points:

$$P = \sum_{n=1}^N A_n \frac{e^{jkr_n}}{r_n}, \quad (1)$$

where A_n denotes amplitude, k is the wave number, and r_n is the propagation distance from point n to $P(x, y)$. Reflecting the Huygens-Fresnel principle, Eq. (1) is highly flexible and physically accurate. Maimone et al. [2017] presented point-source based CGH computation for holographic near-eye displays for virtual and augmented reality. Shi et al. [2021] leveraged point clouds and triangle-ray intersection for occlusion handling in large-scale hologram datasets. However, computational cost scales drastically with point density, and occlusion handling requires additional geometric computations.

Polygon-based CGH balances efficiency and accuracy by representing surfaces using triangular or polygonal facets emitting coherent wave fields. This method naturally integrates shading models and intrinsic occlusion handling through visibility algorithms (e.g. back-face culling and affine transformations) [Matsushima and Nakahara 2009; Zhang et al. 2018b]. Mesh-based CGH includes topology information for precise occlusion handling [Ahrenberg et al. 2008; Yeom et al. 2022]. While achieving realistic shading by combining diffraction with rendering pipelines, these methods suffer from increased algorithmic complexity and struggle with finely detailed or non-polygonal structures.

Layer-based CGH subdivides scenes into discrete depth planes, propagating complex fields from P independently to each plane using operators like Angular Spectrum Method (ASM) [Matsushima and Shimobaba 2009; Zhang et al. 2020; Zheng et al. 2024]. The $P(x, y)$ is optimized so propagated results across all planes approximate the desired 3D scene. This method greatly accelerates computations through Fast Fourier Transform (FFT)-based propagation, making it suitable for faster rendering and widely adopted in learned CGH methods [Choi et al. 2021b; Liu et al. 2023; Peng et al. 2020; Shi et al. 2022; Zhan et al. 2024].

While recent CGH advancements enable realistic defocus effects and continuous pupil accommodation [Kavaklı et al. 2023a; Kim et al. 2024], existing light field-based 3D and 4D CGH methods are typically optimized for narrow viewing directions, with computed phase patterns losing validity under significant geometric changes. We propose integrating strengths of both point-based and layer-based CGH methods, utilizing 3D Gaussians as point-based primitives to encode scene geometry and radiance. Unlike existing Eulerian approaches, our method follows a Lagrangian-based formulation, treating amplitude and phase of light as intrinsic variables to Gaussian primitives. Compared with point clouds and polygon-meshes, Gaussians have learnable scale and rotation parameters, allowing them to capture anisotropic structures and fine-grained spatial variations effectively. This expressiveness supports both appearance modeling and geometrically faithful wave emitter distribution. Table 1 demonstrates our proposed method, enabling fast inference without per-view recalculation, natural defocus blur, on-par image quality, and geometrically aligned phase across novel views.

Method	Inference	Re	Type	Quality	Align	NDB
3DGS + U-Net [2025]	Fast	Yes	Intensity	Good	No	No
GWS [2025]	Moderate	Yes	Complex	Good	No	No
Our Method	Fast	No	Complex	On-par	Yes	Yes

Table 1. Comparison of Gaussian primitives based hologram synthesis method. *Inference* refers to inference speed. *Re* refers to whether the method requires recalculation when geometric relationship between scene and observer changes. *Type* refers to Gaussian representation type. *Quality* refers to the image quality of reconstructed images from the holograms. *Align* refers to geometrically aligned phase across novel views. *NDB* refers to natural defocus blur.

3 Background and Problem Definition

Before explaining our approach, we first introduce the key concepts and terminologies in this paper to define the research problem we

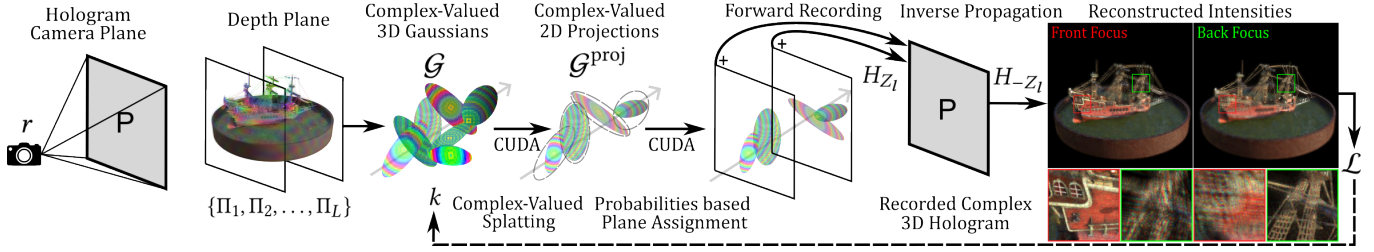


Fig. 3. Without the need for querying from an intensity-based radiance field, our approach models a complex-valued holographic radiance field using Gaussian primitives with intrinsic phase properties, enabling geometrically aligned phase relationships across viewpoints and efficient rendering through a differentiable multi-layer propagation pipeline.

are trying to solve. In this section, we explain several primary components to describe the research problem. These components are: 3D Gaussians for scene representation, hologram planes for wave recording, and camera parameters for view-dependent rendering.

Representing 3D scenes with intensity-based Gaussians. In line with the approach of [Kerbl et al. 2023], we learn geometry and radiance of scenes through the optimization of 3D Gaussians primitives. We consider a 3D region in Euclidean space, $\Omega \subset \mathbb{R}^3$. A scene inside Ω is described using a set of N oriented 3D Gaussians, and each Gaussian is denoted by \mathcal{G}_n . Typically, each \mathcal{G}_n is parameterized by $k = (\mathbf{c}_n, \mathbf{x}_n, \mathbf{R}_n, \mathbf{S}_n, \alpha_n)$, where $\mathbf{c}_n \in \mathbb{R}^3$ represents color, $\mathbf{x}_n \in \mathbb{R}^3$ represents the center point of a Gaussian, $\mathbf{R}_n \in \mathbb{R}^4$ describes the rotation of a Gaussian, \mathbf{S}_n represents scale along principal axes defined by \mathbf{R}_n , and α_n represents the opacity. The *geometrical shape* of a 3D Gaussian is defined as:

$$\mathcal{G}(\mathbf{x}, \mathbf{R}, \mathbf{S}) = \exp\left(-\frac{1}{2} \mathbf{x}^\top \Sigma^{-1} \mathbf{x}\right), \quad (2)$$

where the covariance, Σ , is decomposed into a rotation matrix, \mathbf{R} , and a scaling matrix, \mathbf{S} :

$$\Sigma = \mathbf{R} \mathbf{S} \mathbf{S}^\top \mathbf{R}^\top. \quad (3)$$

We project these 3D Gaussians onto 2D planes to render images at a camera plane, a process also known as the *differential splatting*. The process of differential splatting involves applying the transformation matrix, \mathbf{W} , and the Jacobian projection function, \mathbf{J} , mapping 3D points to 2D image plane. The covariance in camera-space, Σ' , is defined as:

$$\Sigma' = \mathbf{J} \mathbf{W} \Sigma \mathbf{W}^\top \mathbf{J}^\top. \quad (4)$$

For each pixel, the color and opacity contributed by each Gaussian are computed by evaluating Eq. (2) under its learned parameters. The blending of N ordered Gaussians overlapping a given pixel is defined as follows:

$$\mathbf{C}_N = \sum_{n=1}^N \mathbf{c}_n \alpha_n \prod_{j=1}^{n-1} (1 - \alpha_j), \quad (5)$$

where \mathbf{c}_i and α_i represent the color and opacity of the i -th Gaussian.

Hologram Plane, Camera and Problem Definition. We introduce our hologram plane as $P \in \mathbb{C}^{n_x \times n_y}$, where $n_x, n_y \in \mathbb{Z}$. The center of P is co-located with a camera pointing at the center of Ω located at d distance away. We always position P based on the camera pose, location and angles, $r = (x_c, y_c, z_c, \phi_x, \phi_y, \phi_z)$, in the Euler

space. Each complex pixel P_i has a pixel pitch, Δx . Given input $q = (r, \Delta x, n_x, n_y)$, the goal is to obtain the hologram plane by propagating the complex field generated from the Gaussian primitives to the hologram plane $P(q)$:

$$P(q) = U(q) * h, \quad (6)$$

where $U(q)$ denotes the complex field rendered from the Gaussian primitives given camera parameters q , and h is the spatial-domain wave propagation kernel derived from the inverse Fourier transform of the frequency-domain propagation function H [Matsushima and Shimobaba 2009; Zheng et al. 2024]. A common propagation method is the band-limited ASM, where the transfer function $H_z(f_x, f_y)$ encodes propagation by a distance z in the frequency domain:

$$H_z(f_x, f_y) = \begin{cases} \exp(j2\pi z \sqrt{\frac{1}{\lambda^2} - (f_x^2 + f_y^2)}), & \text{if } f_x^2 + f_y^2 \leq \frac{1}{\lambda^2} \\ 0, & \text{otherwise.} \end{cases} \quad (7)$$

In this paper, we also utilize band-limited ASM as the propagation method for complex-valued holographic radiance fields modeling.

4 Method

In this section, we describe our method using the terms defined in Sec. 3. While classical radiance is defined as a scalar energy quantity ($\text{W}/(\text{sr} \cdot \text{m}^2)$) that does not encode phase, our formulation instead models a full complex-valued field, incorporating both amplitude and phase, to capture phenomena such as interference and diffraction. We use the term *complex-valued holographic radiance fields* to maintain conceptual continuity with prior 3D scene representations such as NeRF and 3DGS, while reinterpreting radiance in a wave-optical context. This formulation bridges graphics and optics by embedding coherent light modeling within the familiar structure of radiance fields.

4.1 Complex-Valued Holographic Radiance Fields

We provide an overview of our method in Fig. 3. Given a camera pose, r , and a target hologram plane, P , we partition Ω into multiple planes in depth. At each depth plane, we render our learnable complex-valued 3D Gaussians into corresponding 2D projections. During this projection process, we utilize learnable probabilities to our 3D Gaussians that helps us determine if a 3D Gaussian contributes to that selected depth plane. Note that learning these probabilities in terms of their contributions at each depth plane help to inherently capture depth characteristics of a given scene. Once we determine

the appropriate 2D projections for each layer, we propagate the complex field from each layer towards our camera to construct our P .

Layer Construction. For every 3D Gaussian \mathcal{G}_n with center \mathbf{x}_n , we project its 2D projections to the "most appropriate" plane Π_l , based on learnable probabilities. Let $\{\Pi_1, \Pi_2, \dots, \Pi_L\}$ be a set of discretized parallel planes in the volume, Ω , positioned periodically along the optical axis in front of the view-dependent camera. Each plane Π_l is separated from its neighbors by a fixed depth interval of Δz . The planes span a volume of depth, the center of the volume is placed at a propagation distance, d , from the camera plane. In this arrangement, the entire depth is symmetrically distributed as in the common literature, ranging from: $Z_1 = d - \frac{(L-1)}{2}\Delta z$ to $Z_L = d + \frac{(L-1)}{2}\Delta z$. Each plane Π_l is sampled on a 2D grid that matches the physical resolution of a SLM.

Complex-Valued 3D Gaussian. Consider a multi-plane case where Gaussians are projected onto L numbers of planes $\{\Pi_l\}_{l=1}^L$, we compute each 2D splat via perspective projection of 3D Gaussians following Eq. (4),

$$\mathcal{G}^{\text{proj}}(\mathbf{x}, \mathbf{R}, \mathbf{S}, \mathbf{J}, \mathbf{W}, u) = \exp\left(-\frac{1}{2}(u - \mu)^\top \Sigma'^{-1}(u - \mu)\right), \quad (8)$$

where $u = (n_x, n_y)$ and $\mu = \mathbf{J}\mathbf{W}\mathbf{x}$. To model complex-valued holographic radiance fields, we have to modify the original definition of the 3D Gaussian. **Specifically, each Gaussian is now parameterized by**

$$k = (c_n, \mathbf{x}_n, \mathbf{R}_n, \mathbf{S}_n, \boldsymbol{\alpha}_n, \boldsymbol{\varphi}_n, \mathbf{p}_n), \quad (9)$$

where we add two extra parameters: $\boldsymbol{\varphi}_n \in \mathbb{R}^3$ to represent their inherent phase across wavelengths, and $\mathbf{p}_n \in \mathbb{R}^L$ to represent the plane assignment probabilities, where each element lies in $[0, 1]$. Under this formulation, c_n denotes the inherent wave amplitude, replacing its original interpretation as color. The complex field of each 2D projections U_n then is given by:

$$U_n = c_n \mathcal{G}_n^{\text{proj}} \exp(j\boldsymbol{\varphi}_n). \quad (10)$$

When $L = 0$, plane assignment reduces to a single plane, the \mathbf{p}_n trivially equals 1.0, and the complex-valued holographic radiance field will generate 2D holograms. For the multi-plane case, we convert the pre-activation \mathbf{p}'_n to probabilities via arg-max followed by one-hot encoding, resulting in a hard assignment vector \mathbf{p}_n :

$$\mathbf{p}_n = \text{OneHot}(\arg \max_l \mathbf{p}'_n), \quad (11)$$

$$\text{i.e. } \mathbf{p}_{n,l} = \begin{cases} 1, & \text{if } l = \arg \max_l \mathbf{p}'_n \\ 0, & \text{otherwise.} \end{cases}$$

where $\mathbf{p}_{n,l}$ is the assignment probability of the n -th Gaussian to the l -th depth plane. However, the argmax operation is non-differentiable, which impedes gradient-based training. To address this, we employ the Straight-Through Estimator (STE) that allows gradient propagation through the discrete assignment:

$$\begin{aligned} \text{Forward: } \mathbf{p}_n &= \text{OneHot}(\arg \max_l \mathbf{p}'_n), \\ \text{Backward: } \frac{\partial \mathcal{L}}{\partial \mathbf{p}'_n} &= \frac{\partial \mathcal{L}}{\partial \mathbf{p}_n} \cdot \text{softmax}(\mathbf{p}'_n / \tau), \end{aligned} \quad (12)$$

where τ is the temperature controlling the sharpness of the softmax approximation, in our case, we set $\tau = 0.001$, which makes the softmax function close to argmax operation.

Forward Recording and Inverse Propagation. The final complex field at each plane Π_l is then defined as:

$$U_{\Pi_l} = \sum_{n=1}^N \mathbf{p}_{n,l} U_n \boldsymbol{\alpha}_n \prod_{j=1}^{n-1} (1 - \boldsymbol{\alpha}_j) \mathbf{p}_{j,l}. \quad (13)$$

This formulation ensures each complex-valued 3D Gaussian contributes exclusively to its assigned plane, allowing the framework to learn optimal plane assignments of the Gaussians during training. Unlike the alpha blending used in intensity-based approaches, which indiscriminately mixes RGB colors across all elements, our method creates plane-specific visibility by blending complex values (containing both amplitude and phase information) only among Gaussians assigned to the same depth plane to each pixel. Once each layer Π_l is populated by assigned 2D projections, we use the transfer function H to propagate Π_l towards the hologram plane P , a process we named *Forward Recording* in our framework. This wave-based propagation extends the traditional intensity neural rendering in Eq. (5). Specifically, for every Π_l , a $(n_x^{(l)} \times n_y^{(l)})$ grid of complex samples, we compute:

$$U_{\Pi_l \rightarrow P} = \mathcal{F}^{-1}\{H_{Z_l}(f_x, f_y) \cdot \mathcal{F}\{U_{\Pi_l}\}\}, \quad (14)$$

where Z_l is the distance between depth plane Π_l and the hologram plane P . The forward propagated field $U_{\Pi_l \rightarrow P}$ is then added with the contributions from the other planes to record the final complex 3D hologram:

$$P = \sum_{l=1}^L U_{\Pi_l \rightarrow P}. \quad (15)$$

Since each plane is a 2D raster, the computation cost scales linearly with the number of layers L and is dominated by FFTs of size $n_x^{(l)} \times n_y^{(l)}$. After obtaining P , we propagate P back to each depth plane. The back-propagated complex field $U_{P \rightarrow \Pi_l}$ at depth plane Π_l is computed as:

$$U_{P \rightarrow \Pi_l} = \mathcal{F}^{-1}\{H_{-Z_l}(f_x, f_y) \cdot \mathcal{F}\{P\}\}, \quad (16)$$

where we obtain its intensity $I_l = |U_{P \rightarrow \Pi_l}|^2$ as the final rendered image, we name this process *Inverse Propagation* in our framework. Naively, we can supervise the reconstructed intensities I from back-propagated complex field U against the ground-truth image I_{gt} per depth plane l

$$\mathcal{L}_{MSE} = \frac{1}{L} \sum_{l=1}^L \|I_l - I_{gt,l}\|^2. \quad (17)$$

To further improve the image quality of the defocus region, we utilize two complementary loss functions. First, the reconstruction loss \mathcal{L}_{recon} introduced by Kavakli et al. [2023a], which is computed as

$$\begin{aligned} \mathcal{L}_{recon} &= \frac{1}{L} \sum_{l=1}^L (\|I_l - I_{gt,l}\|^2 \\ &\quad + \|I_l \cdot M_l - I_{gt,l} \cdot M_l\|^2 + \|I_l \cdot I_{gt,l} - I_{gt,l} \cdot I_{gt,l}\|^2), \end{aligned} \quad (18)$$

where M_l is the binary mask for depth plane Π_l generated from the target image and its quantized depth. Additionally, we employ the SSIM loss \mathcal{L}_{SSIM} defined as

$$\mathcal{L}_{SSIM} = \frac{1}{L} \sum_{l=1}^L \lambda_1 \cdot (1 - \text{SSIM}(I_l, I_{gt,l})), \quad (19)$$

where $\lambda_1 = 0.005$. The final training loss is $\mathcal{L} = \mathcal{L}_{recon} + \mathcal{L}_{SSIM}$.

4.2 Fast Differentiable Complex-Valued Rasterizer

Building upon the tile-based architecture from 3DGS, we extend the system to support complex field calculations for holographic rendering while maintaining fast sorting and efficient parallel processing. Our method preserves the core 16×16 tile structure, computing screen-space extents with additional consideration for phase-dependent effects during preprocessing.

For the forward pass, we adapt tile-based rendering to track both real and imaginary components of Gaussians. Each thread block collaboratively loads Gaussian data into shared memory, with threads processing individual pixels by accumulating complex field contributions using fast trigonometric operations. Multi-plane rendering is handled through plane-specific filtering directly in the kernel, skipping Gaussians with low assignment probabilities to minimize thread divergence while supporting depth-dependent complex field accumulation. Per pixel, we track final transmittance and the last contributing Gaussian’s position per plane for correct backward gradients.

The backward pass maintains the same tile-based structure but traverses Gaussians back-to-front, reusing the sorted array from the forward pass with pixels processing only up to their recorded last contributor. This ensures constant memory overhead regardless of scene complexity. We store only the final accumulated opacity per pixel during forward pass, then recover intermediate opacity values during the backward pass by dividing the final opacity by each Gaussian’s contribution, eliminating the need for long opacity lists while enabling accurate gradient computation. This implementation efficiently renders complex-valued holographic radiance fields while retaining the performance benefits of the original tile-based rendering structure. For details of the forward operation and backward gradient computation, please refer to Supplementary Sec. C.

4.3 Geometrically Aligned Phase Modeling

Traditional CGH Methods. A limitation in traditional CGH methods is their dependency on optimizing the complex field for a fixed geometric relationship between the hologram and the 3D scene content. In these methods, a hologram plane $P_0(x, y)$ is designed to encode the entire 3D scene as viewed from a specific geometric configuration, with the complex field at the viewing plane described as:

$$U_0(x', y') = \mathcal{F}^{-1}\{H_z(f_x, f_y) \cdot \mathcal{F}\{P_0(x, y) \cdot R(x, y)\}\}, \quad (20)$$

where $R(x, y)$ is the reference wave. While a properly estimated 3D hologram inherently contains information for different viewing angles within the Space-Bandwidth Product (SBP) limits of the pixel pitch—functioning as a “window” into a virtual world that observers can view from different positions—the issue arises when

the *geometric relationship between the object and the hologram plane changes*. Unlike assuming a stationary or narrowly perturbed observer at the center of projection, any significant movement of the camera plane itself within the 3D world demands recalculating the hologram:

$$P_\theta(x, y) \neq P_0(x, y), \quad (21)$$

where θ represents new geometric configuration when relationship between scene geometry and viewpoint changes. Existing CGH methods estimate, optimize, or calculate closed-form solutions of $P(x, y)$ to produce desired intensity patterns, treating each geometric configuration as an independent optimization problem. As shown in Fig. 2, when the scene-to-hologram relationship changes, the previously computed hologram leads to visuals that are highly distorted, resembling noise. Although neural networks enable efficient recalculation of holograms for new configurations, these learned methods still fail to maintain geometrically aligned phase across different camera and geometric arrangements. Instead, neural networks essentially create a new, unrelated data-driven solution, which lacks interpretability and physical consistency; in real-world scenarios, the phase relationships within the same object remain invariant regardless of its geometric relationship to the observation plane. In traditional intensity-based rasterization, each pixel depends only on a handful of nearby fragments; in CGH, by contrast, every primitive contributes across a large “sub-hologram” footprint on the full resolution hologram, and one must accumulate complex-valued wavefronts from all primitives at all spatial frequencies. Primitive-based methods that maintain physical accuracy (e.g., GWS [2025] or ploygon-based CGH) require proper handling of occlusions and interference effects through complex wavefront accumulation:

$$P(x, y) = \sum_{n=1}^N \mathcal{F}^{-1}\{H_{z_n}(f_x, f_y) \cdot \mathcal{F}\{\mathcal{G}_n(x, y) \cdot \mathcal{T}_n(x, y)\}\}, \quad (22)$$

where $\mathcal{T}_n(x, y)$ represents the accumulated transmittance for occlusion of the n -th primitive. This formulation requires expensive convolution for each primitive across the entire hologram plane, yielding complexity of $O(N_{\text{primitives}} \times N_{\text{freq}} \log N_{\text{freq}})$, where N_{freq} is the total number of frequency bins. To improve efficiency, occlusion effects can be neglected by approximating $\mathcal{T}_n(x, y) \approx 1$:

$$P(x, y) \approx \sum_{n=1}^N \mathcal{F}^{-1}\{H_{z_n}(f_x, f_y) \cdot \mathcal{F}\{\mathcal{G}_n(x, y)\}\}. \quad (23)$$

While this reduces complexity to $O(N_{\text{primitives}} \times N_{\text{freq}})$ and enables better parallelization, it sacrifices accurate occlusion modeling and still requires substantial computation, as each primitive must be re-evaluated across the entire hologram plane. Existing CGH methods follow an Eulerian computational paradigm, where the hologram plane coordinates remain fixed while complex fields are recalculated for each viewpoint.

Geometrically Aligned Phase. In contrast, our approach fundamentally differs by modeling the complex field directly in 3D space using Gaussian primitives with intrinsic phase properties—a Lagrangian perspective where the content remains fixed while the geometric relationship changes. Each complex-valued Gaussian \mathcal{G}_n has an explicitly defined phase parameter φ_n that represents its

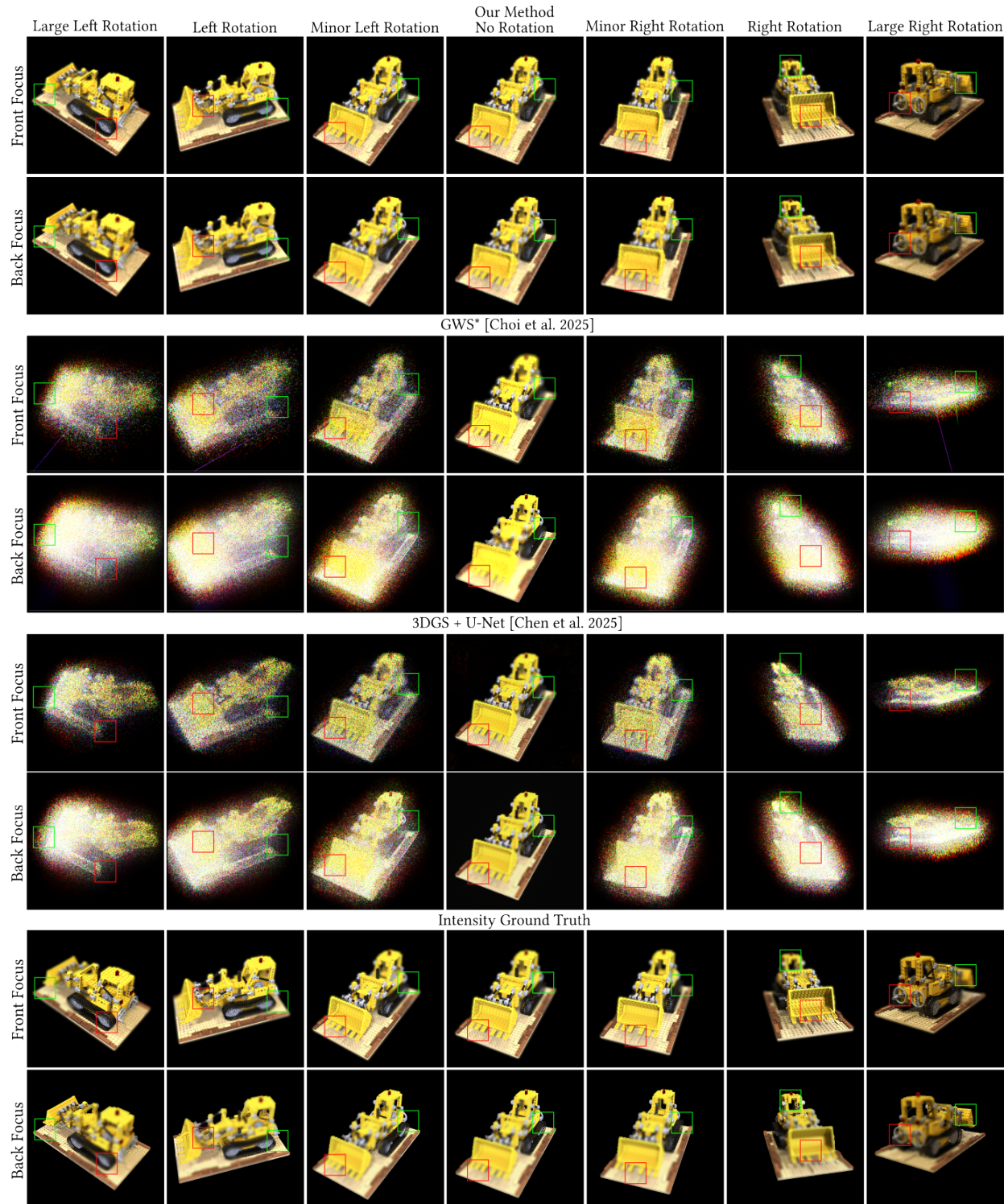


Fig. 4. Comparison of different hologram synthesis methods across different geometric arrangements in simulation. The top row shows our method maintaining geometrically aligned phase from large left to right rotations for novel views. The middle rows show the traditional CGH methods that rely on intensity-based intermediaries, which fail to maintain physical consistency. The bottom row shows the intensity ground truth. * We reimplement the methodology of [Choi et al. 2025] to demonstrate the rotation of single-view propagation results; original non-rotational results show higher image quality than ours.

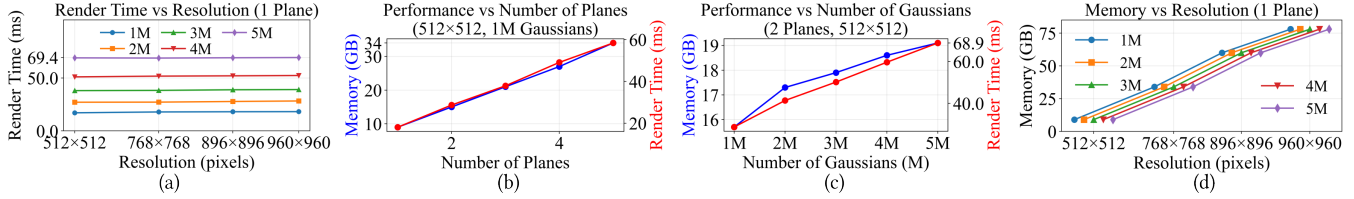


Fig. 5. Performance and memory usage analysis. (a) Render time vs resolution for different Gaussian counts under 1 plane. (b) Memory usage & render time vs number of depth planes. (c) Memory usage & render time vs number of Gaussians. (d) Memory usage vs resolution for different numbers of Gaussians.

inherent holographic properties, independent to camera parameters. The complex field contribution of a Gaussian remains consistent with respect to its 3D position, orientation, and intrinsic phase. This Lagrangian formulation enables us to avoid recalculations in the Eulerian approach, abandons the expensive per-frequency summation, and instead pushes all of the work into two highly optimized GPU-friendly stages: 1. *Tile-based Complex-Valued Rasterization*: As described in Sec. 4.2, by dividing the screen into 16×16 tiles, we extend the 3DGS rasterizer to accumulate complex-valued Gaussians directly in image space and reduce the rasterization cost to $O(N_{\text{primitives}})$. 2. *FFT-based layer propagation*: Instead of summing each primitive’s contribution at every spatial frequency, we collect all Gaussians onto L depth planes once, and then propagate these planes to the hologram plane using 2D FFTs. This reduces the propagation cost to $O(L \times N_{\text{res}} \log N_{\text{res}})$, where $N_{\text{res}} = n_x \times n_y$ is the number of pixels per depth plane, independent to the number of primitives. In this case, since L does not grow with $N_{\text{primitives}}$ and $L \times N_{\text{res}} \log N_{\text{res}}$ is much smaller than $N_{\text{primitives}} \times N_{\text{freq}}$ when the number of primitives is large, our approach achieves inherently better scaling. This results in a more straightforward holographic rendering pipeline that maintains constant propagation cost and geometrically aligned phase regardless of scene complexity. Mathematically, consider two different geometric configurations with respective projection matrices $\mathbf{J}_1, \mathbf{W}_1$ and $\mathbf{J}_2, \mathbf{W}_2$. For a given \mathcal{G}_n , while its projected complex field will differ between geometric configurations, the underlying phase relationship remains consistent:

$$\begin{aligned} U_n^{(1)} &= \mathbf{c}_n \mathcal{G}_n^{\text{proj}}(\mathbf{J}_1, \mathbf{W}_1) \exp(j\varphi_n) \\ U_n^{(2)} &= \mathbf{c}_n \mathcal{G}_n^{\text{proj}}(\mathbf{J}_2, \mathbf{W}_2) \exp(j\varphi_n). \end{aligned} \quad (24)$$

This phase consistency is further maintained through the *Forward Recording* process:

$$P^{(i)} = \sum_{l=1}^L \mathcal{F}^{-1}\{H_{Z_l}(f_x, f_y) \cdot \mathcal{F}\{U_{\Pi_l}^{(i)}\}\}, \quad (25)$$

where $U_{\Pi_l}^{(i)}$ represents the complex field at depth plane Π_l for geometric configuration i , and $P^{(i)}$ is the recorded hologram. As shown in Fig. 4, the significance of the view-consistent phase becomes apparent when examining the reconstructed wavefront across different viewpoints. In real life, light emitted or scattered from a physical point maintains a geometrically aligned phase relationship relative to other points, regardless of the geometric arrangement or observer’s position. Complex-valued holographic radiance field attempts to mimic this physical behavior, ensuring that the

phase differences between scene elements remain invariant, leading to geometrically aligned interference and diffraction effects. This represents a paradigm shift—from treating the phase as a computational convenience applied after intensity determination on the hologram plane, to modeling it as an intrinsic and meaningful property of the scene itself. By combining the Lagrangian perspective of 3DGS with holography, we achieve modeling and rendering of a complex-valued holographic radiance field, eliminating the need for expensive per-configuration, per-primitive wave calculations.

5 Implementation

We employ the ground truth images and rendered depth information to generate target reconstruction images using the multiplane generation pipeline by Kavaklı et al. [2023b]. Additionally, we employ the fused SSIM proposed by [Mallick et al. 2024] to speed up the training process. For densification, we adopt the original strategy from 3DGS, with the exceptions that the densifying frequency is 300 steps and the opacity resetting is replaced by the regularization method proposed by [Rota Bulò et al. 2024].

We choose Adan [Xie et al. 2024] as the optimizer ($\beta_1 = 0.9, \beta_2 = 0.99$) and train our complex-valued Gaussians for 20000 steps using parameter-specific learning rates: 0.005 for scales, 0.0025 for both amplitude and phase, 0.025 for opacity, 0.001 for rotation, and a base learning rate of 0.01 for means and plane assignment probabilities. Our choice of optimizer follows [Zhang et al. 2024], while the learning rate is adopted from the original 3DGS implementation. We apply CosineAnnealingLR [2017] only to the learning rates of means and plane assignment probabilities (minimum 0.00001) for smoother convergence, while keeping the others fixed throughout training. For holographic configuration, we follow the most recent literature [Akşit and Itoh 2023; Shi et al. 2021, 2022] and choose a propagation distance of 2 mm, volume depth of 4 mm, pixel pitch of $3.74 \mu\text{m}$, and wavelengths of 639, 532, and 473 nm.

6 Evaluation

We evaluate our method on three standard datasets to demonstrate its effectiveness, including NeRF Synthetic [Mildenhall et al. 2021], LLFF [Mildenhall et al. 2019], and Mip-NeRF 360 [Barron et al. 2022].

6.1 Baseline Selection

We compare our method against a two-stage method that generates 3D holograms using a U-Net [Ronneberger et al. 2015] from RGBD inputs queried from the pretrained intensity-based 3DGS scene. This two-stage method serves as our baseline for several reasons. First,

Table 2. Performance comparison on NeRF Synthetic and LLFF. GT represents the 3DGS + U-Net (GT), which is *Image Quality Ground Truth* that requires recalculation per viewpoint. 3DGS + U-Net (Vary) represents the *Viewpoint Relationship Variation* without recalculation. Metrics are reported as PSNR/SSIM/LPIPS, respectively. Bold indicates best performance excluding GT baseline. For more information about baselines, please refer to Sec. 6.1.

Method	NeRF Synthetic (Test Resolution 800×800)								Mean
	chair	drums	figus	hotdog	lego	materials	mic	ship	
GT	29.3/0.91/0.13	28.9/0.90/0.14	31.3/0.95/0.10	30.4/0.94/0.15	28.1/0.89/0.15	29.1/0.92/0.14	32.7/0.95/0.10	29.1/0.90/0.18	29.9/0.92/0.14
3DGS + U-Net (Vary)	7.2/0.15/0.71	9.8/0.12/0.77	8.1/0.18/0.72	8.5/0.14/0.85	7.9/0.09/0.81	7.8/0.16/0.75	8.4/0.19/0.79	9.3/0.11/0.79	8.4/0.14/0.77
Our Method	27.6/0.89/0.14	26.1/0.86/0.17	28.0/0.91/0.13	29.1/0.90/0.16	24.3/0.83/0.21	28.3/0.88/0.17	29.2/0.91/0.14	24.9/0.81/0.23	27.1/0.87/0.17

Method	LLFF (Test Resolution 960×640)						Mean	
	fern	flower	fortress	horns	orchids	room		trex
GT	29.6/0.90/0.35	29.4/0.89/0.32	27.4/0.88/0.37	28.8/0.91/0.37	27.5/0.84/0.39	28.9/0.93/0.36	26.1/0.83/0.41	28.3/0.88/0.37
3DGS + U-Net (Vary)	8.3/0.17/0.78	7.1/0.13/0.82	8.8/0.11/0.85	9.2/0.19/0.79	5.7/0.12/0.83	8.9/0.16/0.80	7.4/0.12/0.86	7.9/0.14/0.82
Our Method	27.9/0.78/0.39	28.1/0.80/0.37	25.2/0.73/0.45	26.7/0.79/0.43	25.1/0.73/0.46	27.3/0.81/0.41	24.5/0.75/0.45	26.4/0.77/0.42

Table 3. Comparison of inference times across different Gaussian primitive based hologram synthesis methods at 800×800 resolution.

Method	Number of \mathcal{G} s	Inference Time
Our Method	200K	10 ms
	5M	69 ms
3DGS + U-Net [Chen et al. 2025]	200K	8 ms
	5M	29 ms
GWS (Fast) [Choi et al. 2025]	15K	> 3 s
	200K	> 40 s
	5M	> 15 min
GWS (Exact) [Choi et al. 2025]	15K	> 1 min
	200K	> 13 min
	5M	> 5 hrs

while neural network-based hologram estimation lacks geometrically aligned phase across viewpoints, it achieves millisecond-level inference time that is substantially faster than other CGH methods, such as optimization. Second, although the learned method introduces unnatural defocus effects and suffers from a limited eye box, the network’s denoising capacity helps minimize speckle noise and artifacts commonly found in other CGH methods, resulting in the top metric image quality. This represents the theoretical upper bound of image quality that our method can achieve under ideal conditions. Therefore, we use the 3DGS + U-Net (GT) method as our benchmark, serving as the *Image Quality Ground Truth* against which the performance of our method is evaluated. Additionally, we evaluate the *Viewpoint Relationship Variation* scenario where 3DGS + U-Net generates holograms without recalculation when the relationship between scene geometry and viewpoint changes, named 3DGS + U-Net (Vary).

6.2 Inference Time

Table 3 demonstrates our method’s efficiency. Compared with GWS, our method is inherently more scalable, achieving 30x-10,000x speedup while preserving geometric consistency across novel views. While 3DGS + U-Net offers faster rendering, it requires a re-estimation of the phase per viewpoint, compromising geometric consistency. Even with a large number of Gaussians (5M), our method maintains

reasonable performance (69 ms), achieving a balance between computational efficiency and the representation of a view-consistent complex-valued holographic radiance field. Fig. 5 illustrates the scalability of our method; the render time remains relatively constant across resolutions due to tile-based rasterization, while both memory usage and render time scale linearly with the number of depth planes and Gaussian primitives, demonstrating the computational efficiency of our method compared to traditional CGH methods that rely on per-primitive diffraction calculation.

6.3 Complex Field Discontinuities: Beyond Intensity-Based Smooth Interpolation

6.3.1 Quantitative Analysis. Table 2 and 4 show the training images performance of our method and 3DGS + U-Net on the NeRF Synthetic, LLFF, and Mip-NeRF 360 datasets, respectively. We evaluate the image quality using PSNR, SSIM, and LPIPS [Zhang et al. 2018a].

The *Viewpoint Relationship Variation* results show that 3DGS + U-Net (Vary) fails to generate correct holograms when geometry changes without recalculation, with PSNR dropping by 21.5 dB, 20.4 dB, and 19.6 dB on NeRF Synthetic, LLFF, and Mip-NeRF 360 datasets, respectively, and SSIM decreases by over 0.74 across all 17 scenes. In contrast, our method maintains robust performance under geometric variations, achieving 18.7 dB, 18.5 dB, and 13.9 dB PSNR improvements over 3DGS + U-Net (Vary).

For the *Image Quality Ground Truth*, our method achieves promising performance on the NeRF Synthetic and LLFF datasets, with PSNR gaps of 2.8 dB and 1.9 dB and SSIM differences of 0.05 and 0.11, respectively, compared to 3DGS + U-Net (GT). However, performance degradation of our method becomes significant on Mip-NeRF 360 datasets with 5.7 dB PSNR drop and 0.42 SSIM decrease. This progressive degradation from controlled synthetic scenes to complex in-the-wild environments stems from the fundamental challenge of representing spatially discontinuous complex fields to model interference and diffraction.

6.3.2 Complex Field Discontinuities. In intensity-based radiance fields, the goal is to model view-dependent appearance through opacity and color. This representation handles sparse viewpoint sampling effectively because intensity variations generally follow

smooth, low-frequency patterns that can be interpolated between viewpoints. However, complex-valued holographic radiance fields modeling introduces a challenge related to motion parallax. For a camera translation, motion parallax causes objects at different depths to experience different amounts of apparent displacement. Objects at depths d_1 and d_2 exhibit displacements of:

$$\Delta s_1 = \frac{f \cdot \Delta t}{d_1}, \quad \Delta s_2 = \frac{f \cdot \Delta t}{d_2}, \quad (26)$$

where f is the focal length and Δt is the camera translation. When $d_2 \gg d_1$, the motion parallax difference $\Delta s_1 - \Delta s_2$ becomes significant. This motion parallax translates directly into phase differences in complex-valued holographic radiance fields. Between consecutive camera viewpoints, these primitives accumulate different phase shifts:

$$\Delta \varphi_1 = \frac{2\pi}{\lambda} \Delta s_1, \quad \Delta \varphi_2 = \frac{2\pi}{\lambda} \Delta s_2. \quad (27)$$

The issue arises when adjacent pixels correspond to objects with vastly different depths, creating sharp spatial discontinuities in phase distribution. Consider two Gaussian primitives at depths d_1 and d_2 that are spatially adjacent in the hologram plane, the contrasting phase evolution during camera motion will introduce visual artifacts. For adjacent pixels separated by distance Δx , the spatial phase gradient is defined as:

$$\frac{\partial \varphi}{\partial x} = \frac{\Delta \varphi_2 - \Delta \varphi_1}{\Delta x} = \frac{2\pi f \cdot \Delta t \cdot (d_2 - d_1)}{\lambda d_1 d_2 \Delta x}. \quad (28)$$

When the scene contains large depth discontinuities ($d_2 \gg d_1$), the spatial phase gradient will become very large. This creates interpolation challenges absent in intensity-based representations. Unlike intensity values, which are continuous and monotonic, phase values wrap at 2π boundaries. Large spatial phase gradients cause adjacent pixels to differ by multiple cycles, creating ambiguity in interpolation paths that intensity representations don't encounter. To evaluate our method against complex field discontinuities, we carefully choose and analyze challenging scenes with significant depth variations from commonly used datasets that exhibit different motion parallax characteristics.

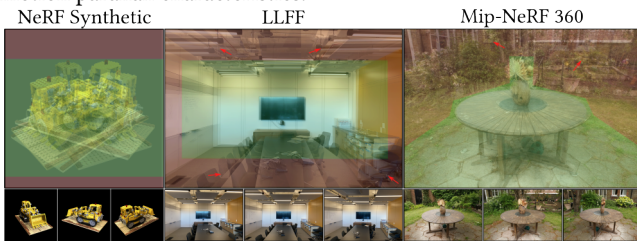


Fig. 6. Motion parallax across datasets: NeRF Synthetic (left) shows a controlled scene with minimal parallax; LLFF (center) shows an indoor scene with vast-moving foreground motion (red region); Mip-NeRF 360 (right) shows an in-the-wild scene with wide background shifts (red region). Regions exhibiting moderate motion parallax that does not cause phase discontinuities in our experiments are marked in green.

As shown in Fig. 6, the NeRF Synthetic dataset benefits from controlled capture conditions with relatively uniform depth distributions within each scene. In contrast, LLFF and Mip-NeRF 360 datasets contain in-the-wild scenes with larger depth variations.

These scenes create sharp phase boundaries where the complex field changes abruptly in between viewpoints, breaking the spatial coherence assumptions of intensity-based representation. While the 3DGS + U-Net method maintains visual quality by first modeling geometry and appearance through intensity-based 3DGS (which handles motion parallax effectively) and then estimating phase as a secondary task, this two-stage approach sacrifices the physical consistency across different geometric configurations. This limitation highlights the trade-off between the spatial coherence requirements of intensity-based representations and the phase discontinuities introduced by motion parallax in holographic radiance fields.

Table 4. Performance comparison on Mip-NeRF 360. GT means the 3DGS + U-Net (GT), which is *Image Quality Ground Truth* that requires recalculation per viewpoint. 3DGS + U-Net (Vary) means the *Viewpoint Relationship Variation* without recalculation. Metrics are reported as PSNR/SSIM/LPIPS, respectively. Bold indicates best performance excluding GT baseline.

Method	Mip-NeRF 360 (Test Resolution 960×640)	
	garden	kitchen
GT	25.9/0.87/0.35	28.1/0.91/0.34
3DGS + U-Net (Vary)	7.9/0.11/0.72	6.9/0.13/0.78
Our Method	20.2/0.45/0.61	22.4/0.49/0.53

6.4 Qualitative Analysis

Defocus Blur Comparison. Fig. 7 compares simulated defocus blur across three CGH methods: optimization, 3DGS + U-Net, and ours. Our method generates perceptually more plausible defocus blur, similar to the optimization-based result without per-view recalculation. 3DGS + U-Net's result suffers from structured, fringing effect in defocus blur, which is commonly found in learned CGH methods [Chen et al. 2025; Shi et al. 2021].

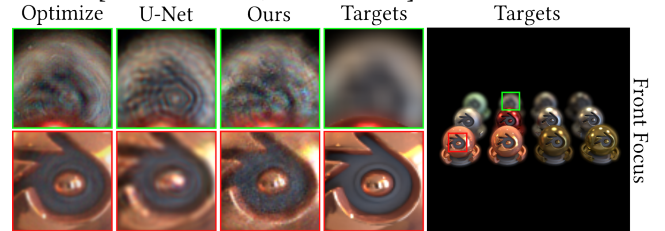


Fig. 7. Defocus blur comparison in holographic reconstructions between optimization [Kavaklı et al. 2023b], 3DGS + U-Net [Chen et al. 2025], and our method against target images.

Novel View Image Quality Analysis. We evaluate novel view image quality on the NeRF Synthetic, LLFF, and Mip-NeRF 360 datasets—shown in Fig. 8, Fig. 9, and Fig. 10, respectively—using both simulation and experimental captures. For NeRF Synthetic dataset, our method achieves visually consistent results across different datasets and on-par image quality compared with the baseline.

For LLFF dataset, our method preserves image quality effectively in regions with stable depth content, particularly for background elements. However, artifacts become apparent in areas containing near-field objects that exhibit rapid motion across viewpoints, such as foreground furniture and close-range structural elements. These artifacts manifest as phase inconsistencies and visual distortions,

primarily in regions where objects undergo significant displacement due to motion parallax.

For Mip-NeRF 360 dataset, the most significant quality loss of our method occurs in distant background regions that experience substantial motion across large viewpoint changes, such as far-field vegetation and architectural structures. Objects at intermediate and near depths maintain reasonable reconstruction quality. This depth-dependent performance indicates that limitations arise from phase discontinuities caused by motion parallax rather than deficiencies in our complex-valued representation, as evidenced by the preserved quality in spatially coherent depth regions. For more simulated and captured result, please refer to Supplementary Sec. D.

Phase-only Hologram Conversion. To display our complex-valued holograms on a phase-only SLM, we leverage a propagation-based optimization approach that converts amplitude-phase into phase-only representations. Given our complex hologram $P = Ae^{j\varphi}$ with amplitude A and phase φ , we aim to obtain a corresponding phase-only hologram $P_\varphi = e^{j\varphi_{\text{opt}}}$ where the amplitude is unity and the phase φ_{opt} is optimized. We propagate both holograms to the same set of depth planes and minimize their propagation differences. For each depth plane Π_l , we compute the propagated complex fields

$$\begin{aligned} U_l &= \mathcal{F}^{-1}\{H_{-z_l}(f_x, f_y) \cdot \mathcal{F}\{P\}\}, \\ U_{\varphi,l} &= \mathcal{F}^{-1}\{H_{-z_l}(f_x, f_y) \cdot \mathcal{F}\{P_\varphi\}\}, \end{aligned} \quad (29)$$

and the optimization minimizes the difference between the real and imaginary components across all depth planes

$$\mathcal{L}_\varphi = \frac{1}{L} \sum_{l=1}^L \|U_l - U_{\varphi,l}\|^2 + \mathcal{L}_{SSIM}(U_l, U_{\varphi,l}). \quad (30)$$

A future version of our method could replace the optimization process with learned approaches, such as U-Net and more, to enable more efficient conversion.

7 Discussion and Future Work

7.1 Limitations

Speed Trade-offs Between CGH and 3DGS. Although our method renders 3D holograms effectively, the rendering process involves splatting Gaussian primitives onto multiple depth planes, followed by wave propagation using the band-limited ASM. The band-limited ASM method is not as efficient as differential splatting, particularly at high resolutions, as it involves multiple high-resolution FFTs to compute accurate wave propagation, which inevitably increases the computation and the memory cost. A more efficient light propagation method is required to further reduce the memory cost and match the rendering speed of intensity-based 3DGS.

Motion Parallax. Our method’s reliance on Gaussian primitives for smooth spatial interpolation creates limitations in scenes with significant motion parallax. Objects at dramatically different depths exhibit varying displacements during viewpoint changes, generating sharp phase discontinuities that violate the smoothness assumptions of intensity-based representations. This explains our degraded results on in-the-wild datasets with large depth variations. Future works could explore hierarchical Gaussians [Wang et al. 2025] to adaptively model phase discontinuities at multiple scales.

Incoherent Illumination. Our method operates under the assumption of fully coherent illumination, where wavefronts exhibit stable phase relationships and produce predictable interference patterns. In contrast, most natural light sources are only partially coherent or incoherent, with phase correlations that degrade over time or across spatial extents. Our model’s reliance on coherent light leads to sensitivity to depth-induced phase artifacts, and partial coherence may help mitigate these discontinuities, highlighting an important direction for future work.

7.2 Future Work

Our work opens the door to potential advances in holographic rendering technology.

Scene Relighting. By directly modeling the complex-valued holographic radiance fields, a future variant of our method could support scene relighting [Guo et al. 2019]. Building on prior research in reflectance displays [Glasner et al. 2014], our approach could extend spatially varying reflectance functions through learned 3D structure and phase information that responds to illumination changes passively and reactively.

Pupil-aware Holography. A future variant could explore estimating complex-valued holographic radiance fields that dynamically adapt to pupil movements under novel views [Chakravarthula et al. 2022]. Moreover, our method inherently contains light field information within the complex-valued 3D representation. With appropriate training objectives, a future extension of our approach could directly support real-time 4D CGH rendering [Kim et al. 2024] without requiring explicit light field extraction.

Time-multiplexed Holography. By performing multiple rounds of optimization on the same scene, it is possible to generate distinct complex-valued radiance variants. These can be displayed in a time-multiplexed fashion using high-speed SLM [Choi et al. 2022] to further enhance the image quality and compensate for the phase discontinuities.

Holographic Camera. Another promising direction lies in bridging synthetic complex-valued holographic radiance fields with real-world holographic acquisition. Recent advances in incoherent holographic cameras [Li et al. 2025; Yu et al. 2023] can capture both intensity and phase information from real 3D scenes under natural illumination without coherent laser sources. Integrating such technology with our framework could enable modeling the true wave optics characteristics of real objects, moving beyond current RGB reproduction to authentic physical phase properties.

Physically Accurate Geometric Alignment. In the physical world, light amplitude is naturally characterized by its spectral distribution, not through mathematical constructs like Spherical Harmonic (SH). To maintain geometrically aligned phase, our complex-valued holographic radiance field uses only RGB triplets to define the intrinsic amplitude of Gaussians to align with the intrinsic phase values. Despite this simplification, our experiments demonstrate that complex-valued holographic radiance field preserves view-dependent reflectance properties of 3D scenes without requiring high-dimensional view-dependent features. Compared to SH, which

typically contains 48 parameters, our method requires only 6 (3 for amplitude, 3 for phase), resulting in reduced model size and memory footprint. Future work is required to investigate the theoretical foundations of this observation and explore if physically plausible parameterizations can further enhance the expressiveness of the radiance fields.

Conclusion. Our work introduces a novel approach to support holographic representations in Gaussian Splatting by utilizing our novel 3D complex-valued Gaussians as primitives. We demonstrate that this method leads to a coherent novel view synthesis that is faithful to the geometry of a 3D scene in terms of both phase and amplitude. These findings from our work demonstrate the potential for more physically accurate 3D scene representations, helping holograms to replace 2D images and holographic displays to be compatible and practical as 3D screens in the future.

References

- Lukas Ahrenberg, Philip Benzie, Marcus Magnor, and John Watson. 2008. Computer generated holograms from three dimensional meshes using an analytic light transport model. *Applied optics* 47, 10 (2008), 1567–1574.
- Kaan Akşit and Yuta Itoh. 2023. HoloBeam: Paper-Thin Near-Eye Displays. In *2023 IEEE Conference Virtual Reality and 3D User Interfaces (VR)*. IEEE, 581–591.
- Jungkwun An, Kanghee Won, Young Kim, Jong-Young Hong, Hojung Kim, Yongkyu Kim, Hoon Song, Chilsung Choi, Yunhee Kim, Juwon Seo, et al. 2020. Slim-panel holographic video display. *Nature communications* 11, 1 (2020), 5568.
- Jonathan T Barron, Ben Mildenhall, Matthew Tancik, Peter Hedman, Ricardo Martin-Brualla, and Pratul P Srinivasan. 2021. Mip-nerf: A multiscale representation for anti-aliasing neural radiance fields. In *Proceedings of the IEEE/CVF international conference on computer vision*. 5855–5864.
- Jonathan T Barron, Ben Mildenhall, Dor Verbin, Pratul P Srinivasan, and Peter Hedman. 2022. Mip-nerf 360: Unbounded anti-aliased neural radiance fields. In *Proceedings of the IEEE/CVF conference on computer vision and pattern recognition*. 5470–5479.
- Jonathan T Barron, Ben Mildenhall, Dor Verbin, Pratul P Srinivasan, and Peter Hedman. 2023. Zip-nerf: Anti-aliased grid-based neural radiance fields. In *Proceedings of the IEEE/CVF International Conference on Computer Vision*. 19697–19705.
- Praneeth Chakravarthula, Seung-Hwan Baek, Florian Schiffers, Ethan Tseng, Grace Kuo, Andrew Maimone, Nathan Matsuda, Oliver Cossairt, Douglas Lanman, and Felix Heide. 2022. Pupil-Aware Holography. *ACM Trans. Graph.* 41, 6, Article 212 (Nov. 2022), 15 pages. <https://doi.org/10.1145/3550454.3555508>
- Praneeth Chakravarthula, Ethan Tseng, Tarun Srivastava, Henry Fuchs, and Felix Heide. 2020. Learned hardware-in-the-loop phase retrieval for holographic near-eye displays. *ACM Trans. Graph.* 39, 6, Article 186 (Nov. 2020), 18 pages. <https://doi.org/10.1145/3414685.3417846>
- Brian Chao, Manu Gopakumar, Suyeon Choi, Jonghyun Kim, Liang Shi, and Gordon Wetzstein. 2024. Large Étendue 3D Holographic Display with Content-adaptive Dynamic Fourier Modulation. In *SIGGRAPH Asia 2024 Conference Papers* (Tokyo, Japan) (SA '24). Association for Computing Machinery, New York, NY, USA, Article 26, 12 pages. <https://doi.org/10.1145/3680528.3687600>
- Gaurav Chaurasia, Sylvain Duchene, Olga Sorkine-Hornung, and George Drettakis. 2013. Depth synthesis and local warps for plausible image-based navigation. *ACM transactions on graphics (TOG)* 32, 3 (2013), 1–12.
- Anpei Chen, Zexiang Xu, Andreas Geiger, Jingyi Yu, and Hao Su. 2022. Tensorf: Tensorial radiance fields. In *European conference on computer vision*. Springer, 333–350.
- Kenneth Chen, Anzhou Wen, Yunxiang Zhang, Praneeth Chakravarthula, and Qi Sun. 2025. View synthesis for 3D computer-generated holograms using deep neural fields. *Optics Express* 33, 9 (2025), 19399–19408.
- Suyeon Choi, Brian Chao, Jacqueline Yang, Manu Gopakumar, and Gordon Wetzstein. 2025. Gaussian Wave Splatting for Computer-Generated Holography. *arXiv preprint arXiv:2505.06582* (2025).
- Suyeon Choi, Manu Gopakumar, Yifan Peng, Jonghyun Kim, Matthew O’Toole, and Gordon Wetzstein. 2022. Time-multiplexed neural holography: a flexible framework for holographic near-eye displays with fast heavily-quantized spatial light modulators. In *ACM SIGGRAPH 2022 Conference Proceedings*. 1–9.
- Suyeon Choi, Manu Gopakumar, Yifan Peng, Jonghyun Kim, and Gordon Wetzstein. 2021a. Neural 3D holography: learning accurate wave propagation models for 3D holographic virtual and augmented reality displays. *ACM Trans. Graph.* 40, 6, Article 240 (Dec. 2021), 12 pages. <https://doi.org/10.1145/3478513.3480542>
- Suyeon Choi, Manu Gopakumar, Yifan Peng, Jonghyun Kim, and Gordon Wetzstein. 2021b. Neural 3d holography: Learning accurate wave propagation models for 3d holographic virtual and augmented reality displays. *ACM Transactions on Graphics (TOG)* 40, 6 (2021), 1–12.
- Daniel Duckworth, Peter Hedman, Christian Reiser, Peter Zhizhin, Jean-François Thibert, Mario Lucić, Richard Szeliski, and Jonathan T Barron. 2024. Smerf: Streamable memory efficient radiance fields for real-time large-scene exploration. *ACM Transactions on Graphics (TOG)* 43, 4 (2024), 1–13.
- Daniel Glasner, Todd Zickler, and Anat Levin. 2014. A reflectance display. *ACM Trans. Graph.* 33, 4, Article 61 (July 2014), 12 pages. <https://doi.org/10.1145/2601097.2601140>
- Joseph W Goodman. 2005. *Introduction to Fourier optics*. Roberts and Company publishers.
- Kaiwen Guo, Peter Lincoln, Philip Davidson, Jay Busch, Xueming Yu, Matt Whalen, Geoff Harvey, Sergio Orts-Escolano, Rohit Pandey, Jason Dourgarian, Danhang Tang, Anastasia Tkach, Adarsh Kowdle, Emily Cooper, Mingsong Dou, Sean Fanello, Graham Fyffe, Christoph Rhemann, Jonathan Taylor, Paul Debevec, and Shahram Izadi. 2019. The relightables: volumetric performance capture of humans with realistic relighting. *ACM Trans. Graph.* 38, 6, Article 217 (Nov. 2019), 19 pages. <https://doi.org/10.1145/3355089.3356571>
- Peter Hedman, Suhub Alsisan, Richard Szeliski, and Johannes Kopf. 2017. Casual 3D photography. *ACM Transactions on Graphics (TOG)* 36, 6 (2017), 1–15.
- M Hossein Eybposh, Nicholas W Caira, Mathew Atisa, Praneeth Chakravarthula, and Nicolas C Pégard. 2020. DeepCGH: 3D computer-generated holography using deep learning. *Optics Express* 28, 18 (2020), 26636–26650.
- Koray Kavakli, Yuta Itoh, Hakan Urey, and Kaan Akşit. 2023a. Realistic defocus blur for multiplane computer-generated holography. In *2023 IEEE Conference Virtual Reality and 3D User Interfaces (VR)*. IEEE, 418–426.
- Koray Kavakli, Liang Shi, Hakan Urey, Wojciech Matusik, and Kaan Akşit. 2023b. Multi-color Holograms improve Brightness in Holographic Displays. In *ACM SIGGRAPH ASIA 2023 Conference Proceedings*. ACM, Sydney, NSW, Australia, -. <https://doi.org/10.1145/3610548.3618135>
- Koray Kavakli, Hakan Urey, and Kaan Akşit. 2022. Learned holographic light transport. *Applied Optics* 61, 5 (2022), B50–B55.
- Bernhard Kerbl, Georgios Kopanas, Thomas Leimkühler, and George Drettakis. 2023. 3D Gaussian splatting for real-time radiance field rendering. *ACM Trans. Graph.* 42, 4 (2023), 139–1.
- Dongyeon Kim, Seung-Woo Nam, Suyeon Choi, Jong-Mo Seo, Gordon Wetzstein, and Yoonchan Jeong. 2024. Holographic parallax improves 3D perceptual realism. *ACM Transactions on Graphics (TOG)* 43, 4 (2024), 1–13.
- Youngeun Kim, Wonjoon Jin, Sunghyun Cho, and Seung-Hwan Baek. 2023. Neural spectro-polarimetric fields. In *SIGGRAPH Asia 2023 Conference Papers*. 1–11.
- Zhao-Song Li, Chao Liu, Xin-Wei Li, Huan Yu, Di Wang, and Qiong-Hua Wang. 2025. Real-time holographic camera for obtaining real 3D scene hologram. *Light: Science & Applications* 14, 1 (2025), 74. <https://doi.org/10.1038/s41377-024-01730-9>
- Kexuan Liu, Jiachen Wu, Zehao He, and Liangcai Cao. 2023. 4K-DMDNet: diffraction model-driven network for 4K computer-generated holography. *Opto-Electronic Advances* 6, 5 (2023), 220135–1.
- Ilya Loshchilov and Frank Hutter. 2017. SGDR: Stochastic Gradient Descent with Warm Restarts. In *5th International Conference on Learning Representations, ICLR 2017, Toulon, France, April 24–26, 2017, Conference Track Proceedings*. OpenReview.net. <https://openreview.net/forum?id=Skq89Scxx>
- Andrew Maimone, Andreas Georgiou, and Joel S Kollin. 2017. Holographic near-eye displays for virtual and augmented reality. *ACM Transactions on Graphics (TOG)* 36, 4 (2017), 1–16.
- Saswat Subhajiyo Mallick, Rahul Goel, Bernhard Kerbl, Markus Steinberger, Francisco Vicente Carrasco, and Fernando De La Torre. 2024. Taming 3DGS: High-Quality Radiance Fields with Limited Resources. In *SIGGRAPH Asia 2024 Conference Papers (SA '24)*. Association for Computing Machinery, New York, NY, USA, Article 2, 11 pages. <https://doi.org/10.1145/3680528.3687694>
- Kyoji Matsushima and Sumio Nakahara. 2009. Extremely high-definition full-parallax computer-generated hologram created by the polygon-based method. *Applied optics* 48, 34 (2009), H54–H63.
- Kyoji Matsushima and Tomoyoshi Shimobaba. 2009. Band-limited angular spectrum method for numerical simulation of free-space propagation in far and near fields. *Optics express* 17, 22 (2009), 19662–19673.
- Ben Mildenhall, Pratul P. Srinivasan, Rodrigo Ortiz-Cayon, Nima Khademi Kalantari, Ravi Ramamoorthi, Ren Ng, and Abhishek Kar. 2019. Local Light Field Fusion: Practical View Synthesis with Prescriptive Sampling Guidelines. *ACM Transactions on Graphics (TOG)* (2019). <https://bmlid.github.io/lflf/>
- Ben Mildenhall, Pratul P Srinivasan, Matthew Tancik, Jonathan T Barron, Ravi Ramamoorthi, and Ren Ng. 2021. Nerf: Representing scenes as neural radiance fields for view synthesis. *Commun. ACM* 65, 1 (2021), 99–106.
- Michael Niemeyer, Fabian Manhardt, Marie-Julie Rakotosaona, Michael Oechsle, Daniel Duckworth, Rama Gosula, Keisuke Tateno, John Bates, Dominik Kaeser, and Federico

- Tombari. 2024. Radsplat: Radiance field-informed gaussian splatting for robust real-time rendering with 900+ fps. *arXiv preprint arXiv:2403.13806* (2024).
- Yifan Peng, Suyeon Choi, Nitish Padmanaban, and Gordon Wetzstein. 2020. Neural holography with camera-in-the-loop training. *ACM Transactions on Graphics (TOG)* 39, 6 (2020), 1–14.
- Daniel Rebain, Wei Jiang, Soroosh Yazdani, Ke Li, Kwang Moo Yi, and Andrea Tagliaschi. 2021. DeRF: Decomposed Radiance Fields. In *Proceedings of the IEEE/CVF Conference on Computer Vision and Pattern Recognition (CVPR)*. 14153–14161.
- Gernot Riegler and Vladlen Koltun. 2020. Free view synthesis. In *Computer Vision—ECCV 2020: 16th European Conference, Glasgow, UK, August 23–28, 2020, Proceedings, Part XIX 16*. Springer, 623–640.
- Olaf Ronneberger, Philipp Fischer, and Thomas Brox. 2015. U-net: Convolutional networks for biomedical image segmentation. In *Medical image computing and computer-assisted intervention—MICCAI 2015: 18th international conference, Munich, Germany, October 5–9, 2015, proceedings, part III 18*. Springer, 234–241.
- Samuel Rota Bulò, Lorenzo Porzi, and Peter Kotschieder. 2024. Revising densification in gaussian splatting. In *European Conference on Computer Vision*. Springer, 347–362.
- Florian Schiffrers, Praneeth Chakravarthula, Nathan Matsuda, Grace Kuo, Ethan Tseng, Douglas Lanman, Felix Heide, and Oliver Cossairt. 2023. Stochastic Light Field Holography. *IEEE International Conference on Computational Photography (ICCP)* (2023).
- Liang Shi, Beichen Li, Changil Kim, Petr Kellnhofer, and Wojciech Matusik. 2021. Towards real-time photorealistic 3D holography with deep neural networks. *Nature* 591, 7849 (2021), 234–239.
- Liang Shi, Beichen Li, and Wojciech Matusik. 2022. End-to-end learning of 3d phase-only holograms for holographic display. *Light: Science & Applications* 11, 1 (2022), 247.
- Shlomi Steinberg, Ravi Ramamoorthi, Benedikt Bitterli, Eugene d’Eon, Ling-Qi Yan, and Matt Pharr. 2024. A Generalized Ray Formulation For Wave-Optical Light Transport. *ACM Trans. Graph.* 43, 6, Article 241 (Nov. 2024), 15 pages. <https://doi.org/10.1145/3687902>
- Shlomi Steinberg, Pradeep Sen, and Ling-Qi Yan. 2022. Towards practical physical-optics rendering. *ACM Trans. Graph.* 41, 4, Article 132 (July 2022), 24 pages. <https://doi.org/10.1145/3528223.3530119>
- Yujie Wang, Baoquan Chen, and Praneeth Chakravarthula. 2024. Pupil-Adaptive 3D Holography Beyond Coherent Depth-of-Field. *arXiv preprint arXiv:2409.00028v1* (2024).
- Yifan Wang, Peishan Yang, Zhen Xu, Jiaming Sun, Zhanhua Zhang, Yong Chen, Hujun Bao, Sida Peng, and Xiaowei Zhou. 2025. FreeTimeGS: Free Gaussian Primitives at Anytime Anywhere for Dynamic Scene Reconstruction. In *CVPR*. <https://zju3dv.github.io/freetimegs>
- Xingyu Xie, Pan Zhou, Huan Li, Zhouchen Lin, and Shuicheng Yan. 2024. Adan: Adaptive Nesterov Momentum Algorithm for Faster Optimizing Deep Models. *IEEE Transactions on Pattern Analysis and Machine Intelligence* (2024).
- Han-Ju Yeom, Sanghoon Cheon, Kyunghee Choi, and Joongki Park. 2022. Efficient mesh-based realistic computer-generated hologram synthesis with polygon resolution adjustment. *ETRI Journal* 44, 1 (2022), 85–93.
- Hyeonseung Yu, Youngrok Kim, Daeho Yang, Wontaek Seo, Yunhee Kim, Jong-Young Hong, Hoon Song, Geeyoung Sung, Younghun Sung, Sung-Wook Min, and Hong-Seok Lee. 2023. Deep learning-based incoherent holographic camera enabling acquisition of real-world holograms for holographic streaming system. *Nature Communications* 14, 1 (2023), 3534. <https://doi.org/10.1038/s41467-023-39329-0>
- Yicheng Zhan, Liang Shi, Wojciech Matusik, Qi Sun, and Kaan Akşit. 2024. Configurable Learned Holography. *arXiv e-prints* (2024), arXiv-2405.
- Richard Zhang, Phillip Isola, Alexei A. Efros, Eli Shechtman, and Oliver Wang. 2018a. The Unreasonable Effectiveness of Deep Features as a Perceptual Metric. In *2018 IEEE Conference on Computer Vision and Pattern Recognition, CVPR 2018, Salt Lake City, UT, USA, June 18–22, 2018*. Computer Vision Foundation / IEEE Computer Society, 586–595. <https://doi.org/10.1109/CVPR.2018.00068>
- Wenhui Zhang, Hao Zhang, and Guofan Jin. 2020. Band-extended angular spectrum method for accurate diffraction calculation in a wide propagation range. *Optics letters* 45, 6 (2020), 1543–1546.
- Xinjie Zhang, Xingtong Ge, Tongda Xu, Dailian He, Yan Wang, Hongwei Qin, Guo Lu, Jing Geng, and Jun Zhang. 2024. Gaussianimage: 1000 fps image representation and compression by 2d gaussian splatting. In *European Conference on Computer Vision*. Springer, 327–345.
- Ya-Ping Zhang, Fan Wang, Ting-Chung Poon, Shuang Fan, and Wei Xu. 2018b. Fast generation of full analytical polygon-based computer-generated holograms. *Optics express* 26, 15 (2018), 19206–19224.
- Chuanjun Zheng, Yicheng Zhan, Liang Shi, Ozan Cakmakci, and Kaan Akşit. 2024. Focal Surface Holographic Light Transport using Learned Spatially Adaptive Convolutions. In *SIGGRAPH Asia 2024 Technical Communications (SA '24)*. Association for Computing Machinery, New York, NY, USA, Article 28, 4 pages. <https://doi.org/10.1145/3681758.3697989>

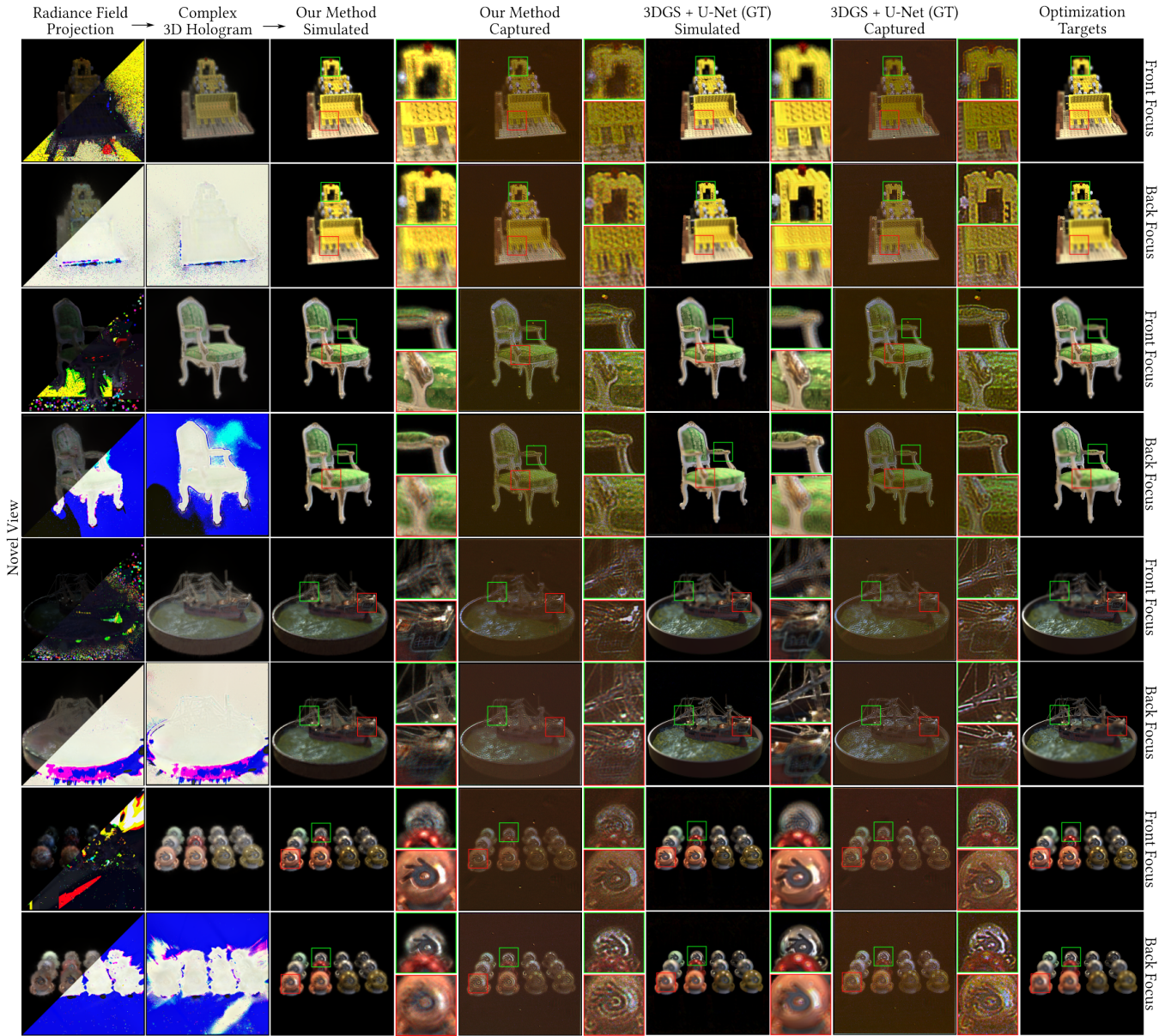


Fig. 8. Novel-view comparison between our method and the 3DGS + U-Net baseline on multiple scenes from the NeRF Synthetic dataset (lego, chair, ship, materials). Here GT represents the *Image Quality Ground Truth*. The first two columns show the radiance field projections and their rendered complex 3D holograms. The central columns present a side-by-side evaluation of our method’s simulated results and experimentally captured results against the baseline. The rightmost column displays the target images used as optimization objectives in our method.

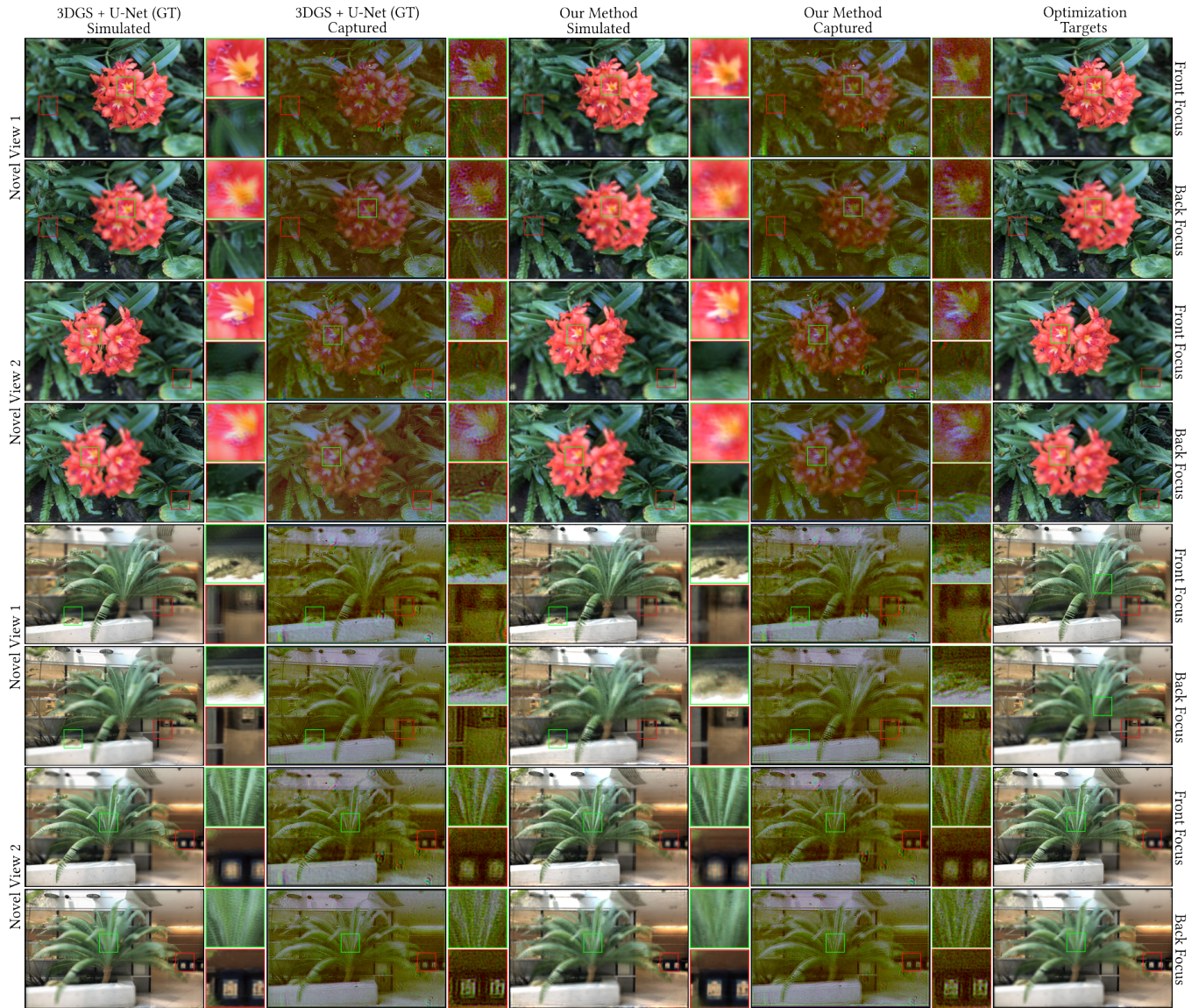


Fig. 9. Novel-view comparison between our method and the 3DGS + U-Net baseline on multiple scenes from the LLFF dataset (flower, fern). Here GT represents the *Image Quality Ground Truth*. The central columns present a side-by-side evaluation of our method's simulated results and experimentally captured results against the baseline. The rightmost column displays the target images used as optimization objectives in our method.



Fig. 10. Novel-view comparison of our method on multiple scene from the Mip-NeRF 360 Synthetic dataset (garden, kitchen). The first two columns show the radiance field projections and their rendered complex 3D holograms. The central columns present our method and 3DGS + U-Net’s simulated results. The rightmost column displays the target images used as optimization objectives in our method.

Supplementary Material

A Hardware Image

Fig. 11 shows the photograph of the holographic display prototype we used in this paper. The optical path of our display prototype begins with a laser light source (LASOS MCS4), which integrates three individual laser lines. The emitted light from a single-mode fibre is collimated using a Thorlabs LA1708-A plano-convex lens with a 200 mm focal length. This linearly polarized, collimated beam is then directed by a beamsplitter (Thorlabs BP245B1) toward our phase-only SLM, the Jasper JD7714 (2400×4094, 3.74 μm). The modulated beam subsequently passes through a lens system comprising Thorlabs LA1908-A and LB1056-A, with focal lengths of 500 mm and 250 mm, respectively. Following this, a pinhole aperture (Thorlabs SM1D12) is positioned at the focal plane of the lenses. Finally, we capture the holographic reconstructions using a lensless image sensor (Point Grey GS3-U3-23S6M-C USB 3.0), which is mounted on an X-stage (Thorlabs PT1/M) with a travel range of 0 to 25 mm and a positioning precision of 0.01 mm.

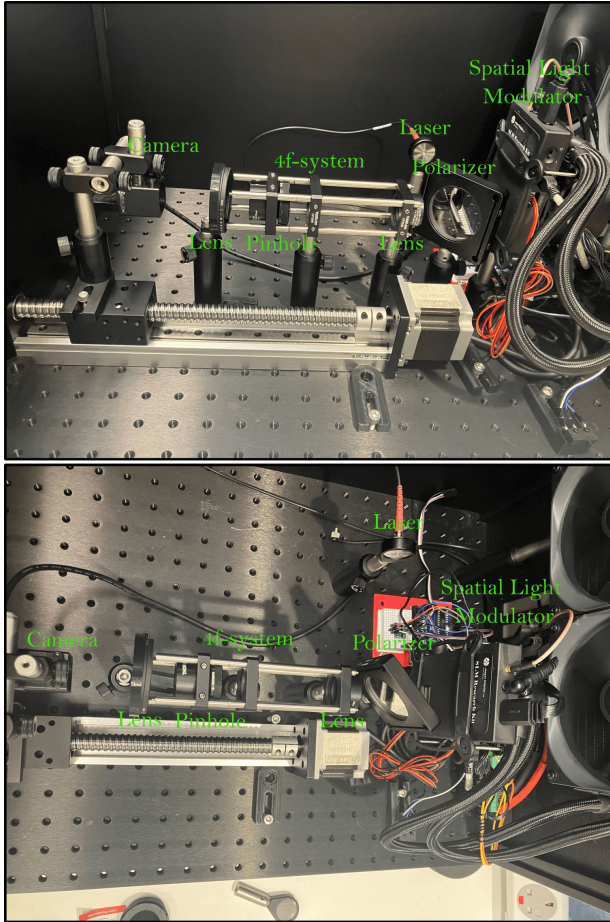


Fig. 11. The photograph of the holographic display prototype (Jasper JD7714) used in evaluating holograms generated by our model.

B Wave Propagation

In this section, we provide additional insights into the implementation of our proposed complex-valued holographic radiance field.

B.1 Wave Propagation From a Single 3D Gaussian Primitive

Each Gaussian \mathcal{G}_n can be considered as a small volume in Ω that emits a coherent wavefield. Intuitively, we may approximate the total field from \mathcal{G}_n at hologram pixel P_i 's coordinate (x, y) by an integral of infinitesimal point contributions at the surface of the Gaussian. **To simplify the problem, if we only consider \mathcal{G}_n 's center at $\mathbf{x}_n = (X_n, Y_n, Z_n)$** , the distance D_n from the \mathcal{G}_n to the hologram pixel at (x, y) is

$$D_n = \sqrt{(x - X_n)^2 + (y - Y_n)^2 + Z_n^2} \quad (31)$$

For a point light source emitting spherical waves, the phase at the hologram pixel is

$$\varphi_n^{\text{prop}} = \frac{2\pi}{\lambda} D_n \pmod{2\pi} \quad (32)$$

Under paraxial approximation, phase can be described using a quadratic function

$$\varphi_n^{\text{approx}} = \frac{2\pi}{\lambda} \left(Z_n + \frac{(x - X_n)^2 + (y - Y_n)^2}{2Z_n} \right) \pmod{2\pi} \quad (33)$$

The resulting complex field from Gaussian \mathcal{G}_n at the hologram pixel is

$$U_n = A_n \exp(j\varphi_n^{\text{prop}}), \quad A_n = \mathbf{c}_n \boldsymbol{\alpha}_n \quad (34)$$

where A_n includes the Gaussian's $\boldsymbol{\alpha}_n$ weighted amplitude, and \mathbf{c}_n represents the inherent wave amplitude of the Gaussian. The full complex field integration of \mathcal{G}_n can be derived by expanding this point response to the Gaussian's spatial extent \mathcal{S}_n and rotation \mathbf{R}_n by densely discretizing the surface of the Gaussian. This yields a volume of wavefront footprint recorded at the hologram plane P . Without considering the occlusion, the total field at the hologram pixel can be defined as:

$$U^{\text{total}} = \sum_{n=1}^N U_n \quad (35)$$

One may average over the sub-samples to compute the field at hologram pixel P_i , or keeping them explicit for higher accuracy modeling.

B.2 Occlusion Aware Field Recording.

In a pure intensity world, to account for fore-ground occlusion, the frontmost Gaussian along the line of sight tends to occlude anything behind it, and people apply alpha-blending to represent transparent pixels. For simulating physical wave propagation in a hologram, occlusion is subtler—each "surface" can block or partially block wavefronts behind it. One approach to accurately model occlusion is to reconstruct a triangle surface mesh by connecting the neighboring points of Gaussians and performing ray casting from each point to the hologram plane P . The wavefronts carried by rays that hit the surface mesh are excluded from the hologram calculation. A binary visibility mask can be generated from this process to mimic foreground-occlusion at the hologram plane. However,

both point-based wave simulation and ray-triangle detection of the entire scene are computationally expensive, making them a less favorable choice in real-time inference. As illustrated in Fig. 12, in our implementation, we use alpha-blending with transmittance to efficiently approximate occlusion effects, each 3D Gaussian \mathcal{G}_n can be considered as a small volume in Ω that emits a coherent wavefield. rather than the more computationally expensive ray-casting approach described above.

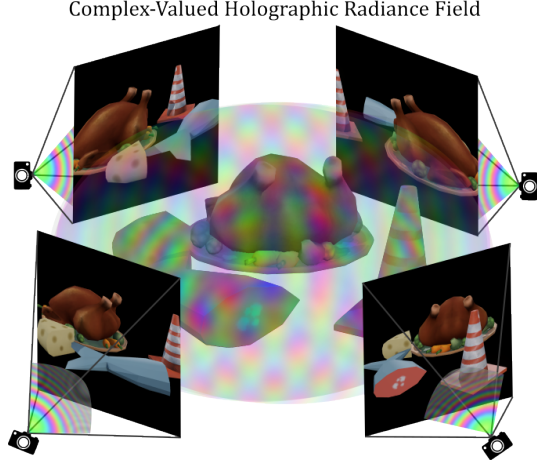


Fig. 12. Our method assumes the radiance field is a wave emitter, instead of a ray tracer.

C Differentiable Complex-Valued Gaussian Rendering

In this section, we provide the pseudo code and a detailed exposition of both the forward computation and the backward gradient derivation for our Differentiable Complex-Valued Rasterizer.

C.1 Notation

- $\mathbf{x}_n \in \mathbb{R}^3$ - 3D Gaussian center positions in world space
- $\mathbf{x}_n^{\text{proj}} \in \mathbb{R}^2$ - Projected 2D Gaussian centers in screen space
- μ_x, μ_y - Components of the 2D mean position
- $\Sigma \in \mathbb{R}^{3 \times 3}$ - 3D covariance matrix in world space
- $\Sigma' \in \mathbb{R}^{2 \times 2}$ - 2D covariance matrix in screen space
- $\Sigma'_{ij}{}^{-1}$ - Elements of the inverse 2D covariance matrix (where $i, j \in \{0, 1\}$)
- $d_x = x - \mu_x, d_y = y - \mu_y$ - Distance from pixel to Gaussian center
- $\mathbf{p}_{n,l}$ - Plane assignment probability of Gaussian n for plane l (controls contribution to each rendering plane)
- φ_n - Phase value for Gaussian n (controls complex field phase)
- α_n - Opacity value for Gaussian n
- α_n^{base} - Base opacity value before applying the Gaussian function
- T_n - Accumulated transmittance at Gaussian n (product of previous transparency values)
- z_{norm} - Normalized depth value between 0 and 1

C.2 Optimization and Densification Algorithm

Our optimization and densification algorithms extend the standard 3DGS [Kerbl et al. 2023] approach to handle complex-valued parameters and multi-plane assignments. The key modifications include phase parameter optimization, plane probability learning with STE, and complex-valued loss computation as summarized in Algorithm 1.

Algorithm 1 Optimization and Densification for Complex-Valued 3DGS

Require: w, h : width and height of the training images
Require: L : number of depth planes for multi-plane rendering

```

1:  $M \leftarrow$  SfM Points ▷ Positions
2:  $S, C, \alpha \leftarrow$  InitAttributes() ▷ Scales, Amplitudes, Opacities
3:  $\varphi \leftarrow$  InitPhase() ▷ Phase Parameters
4:  $\mathbf{p}' \leftarrow$  InitPlaneProbs( $L$ ) ▷ Plane Assignment Logits
5:  $i \leftarrow 0$  ▷ Iteration Count
6: while not converged do
7:    $V, I \leftarrow$  SampleTrainingView() ▷ Camera  $V$  and Image
8:    $\mathbf{p} \leftarrow$  STE( $\mathbf{p}'$ ) ▷ Hard Assignment via STE
9:    $U_{\text{complex}} \leftarrow$  ComplexRasterize( $M, S, C, \alpha, \varphi, \mathbf{p}, V$ ) ▷ Alg. 2
10:   $P \leftarrow$  PropagateToHologram( $U_{\text{complex}}$ ) ▷ Multi-plane ASM
11:   $I_{\text{recon}} \leftarrow$  BackPropagate( $P$ ) ▷ Reconstruct Images
12:   $\mathcal{L} \leftarrow$  ComplexLoss( $I, I_{\text{recon}}$ ) ▷  $\mathcal{L}_{\text{recon}} + \mathcal{L}_{\text{SSIM}}$ 
13:   $M, S, C, \alpha, \varphi, \mathbf{p}' \leftarrow$  Adan( $\nabla \mathcal{L}$ ) ▷ Backprop & Step
14:  if IsRecentIteration() then
15:    for all Gaussians  $(\mu, \Sigma, c, \alpha, \varphi, \mathbf{p}')$  in  $(M, S, C, \alpha, \varphi, \mathbf{p}')$  do
16:      if  $\alpha < \epsilon$  or IsTooLarge( $\mu, \Sigma, c, \alpha$ ) then ▷ Pruning
17:        RemoveGaussian()
18:      end if
19:      if  $\nabla_{\mu} \mathcal{L} > \tau_p$  then ▷ Densification
20:        if  $\|S\| > \tau_s$  then ▷ Over-reconstruction
21:          SplitGaussian( $\mu, \Sigma, c, \alpha, \varphi, \mathbf{p}'$ )
22:        else ▷ Under-reconstruction
23:          CloneGaussian( $\mu, \Sigma, c, \alpha, \varphi, \mathbf{p}'$ )
24:        end if
25:      end if
26:    end for
27:  end if
28:   $i \leftarrow i + 1$ 
29: end while

```

The key extensions to the standard algorithm include: (1) Phase parameter φ initialization with random values in $[0, 2\pi)$; (2) Plane assignment probabilities \mathbf{p}' initialized uniformly and converted to hard assignments via STE during forward pass; (3) Complex-valued rasterization producing multi-plane complex fields; (4) Hologram generation through multi-plane ASM propagation; (5) Phase-aware densification where both split and clone operations preserve phase relationships by adding small random perturbations to maintain coherent interference patterns.

C.3 Details of the Rasterizer

Our tile-based rasterizer extends the standard 3DGS approach to handle complex-valued rendering across multiple depth planes. The algorithm processes Gaussians in back-to-front order within each tile to ensure correct alpha blending for wave-optical effects, as detailed in Algorithm 2.

The rasterizer incorporates several key innovations: (1) Back-to-front depth sorting using inverted depth keys to ensure proper alpha blending for wave propagation; (2) Multi-plane rendering where each Gaussian contributes to planes based on learned assignment probabilities $\mathbf{p}_{g,l}$; (3) Complex field accumulation using amplitude-weighted trigonometric functions $C_g \cdot \cos(\varphi_g)$ and $C_g \cdot \sin(\varphi_g)$ for real and imaginary components; (4) Plane-specific early termination

Algorithm 2 Complex-Valued Tile-Based Rasterization

Require: w, h : width and height of the image to rasterize
Require: M, S : Gaussian means and covariances in world space
Require: C, α, φ, p : Amplitudes, opacities, phases, and plane assignments
Require: V : view configuration of current camera
Require: L : number of depth planes

```

1: function COMPLEXRASTERIZE( $w, h, M, S, C, \alpha, \varphi, p, V$ )
2:   CullGaussians( $M, V$ )                                ▶ Frustum Culling
3:    $M', S' \leftarrow$  ScreenspaceGaussians( $M, S, V$ )      ▶ Transform
4:    $T \leftarrow$  CreateTiles( $w, h$ )                       ▶  $16 \times 16$  Tiles
5:    $I, \mathcal{K} \leftarrow$  DuplicateWithDepthKeys( $M', T$ )     ▶ Back-to-Front Keys
6:    $\mathcal{K}_s, \mathcal{I}_s \leftarrow$  SortByKeys( $I, \mathcal{K}$ )             ▶ Depth Sort
7:    $\mathcal{R} \leftarrow$  IdentifyTileRanges( $T, \mathcal{K}_s$ )            ▶ Tile Ranges
8:    $U_{\text{real}}, U_{\text{imag}} \leftarrow$  InitComplexCanvas( $L, w, h$ ) ▶ Multi-plane Output
9:   for all Tiles  $t$  in  $T$  do
10:    for all Planes  $l$  in  $L$  do
11:     for all Pixels  $\text{pix}$  in  $t$  do
12:       $T_{\text{acc}} \leftarrow 1.0$                             ▶ Transmittance
13:       $\text{real}_{\text{acc}}, \text{imag}_{\text{acc}} \leftarrow 0.0, 0.0$       ▶ Complex Accumulation
14:       $\text{range} \leftarrow$  GetTileRange( $\mathcal{R}, t$ )
15:      for  $g$  in  $\text{range}$  do                               ▶ Back-to-Front Order
16:        $w_{\text{plane}} \leftarrow p_{g,l}$                        ▶ Plane Assignment
17:       if  $w_{\text{plane}} < \epsilon_{\text{plane}}$  then
18:        continue
19:       end if
20:        $\alpha_{\text{eff}} \leftarrow \alpha_g \cdot \exp(-\text{power}_{g,\text{pix}}) \cdot w_{\text{plane}}$  ▶ Effective Alpha
21:        $\text{scale} \leftarrow C_g \cdot \alpha_{\text{eff}} \cdot T_{\text{acc}}$    ▶ Complex Scale
22:        $\text{real}_{\text{acc}} \leftarrow \text{real}_{\text{acc}} + \text{scale} \cdot \cos(\varphi_g)$  ▶ Real Component
23:        $\text{imag}_{\text{acc}} \leftarrow \text{imag}_{\text{acc}} + \text{scale} \cdot \sin(\varphi_g)$  ▶ Imaginary Component
24:        $T_{\text{acc}} \leftarrow T_{\text{acc}} \cdot (1 - \alpha_{\text{eff}})$  ▶ Update Transmittance
25:       if  $T_{\text{acc}} < \epsilon_T$  then
26:        break                                          ▶ Early Termination
27:       end if
28:       end for
29:        $U_{\text{real}}[l, \text{pix}] \leftarrow \text{real}_{\text{acc}}$ 
30:        $U_{\text{imag}}[l, \text{pix}] \leftarrow \text{imag}_{\text{acc}}$ 
31:     end for
32:   end for
33: end for
34: return  $U_{\text{real}} + j \cdot U_{\text{imag}}$ 
35: end function

```

when transmittance falls below threshold ϵ_T ; (5) Efficient shared memory usage for tile-based processing with complex-valued intermediate storage.

D Extra Simulated And Captured Result

This section presents additional experimental results demonstrating the effectiveness of our complex-valued 3D Gaussian splatting approach across diverse scenes. We provide comprehensive comparisons on both synthetic and real-world datasets, including scenes from the NeRF Synthetic dataset (lego in Fig. 13, chair in Fig. 14, ship in Fig. 15, materials in Fig. 16, and hotdog in Fig. 17) and the LLFF dataset (flower in Fig. 18, fern in Fig. 19, trex in Fig. 20, and room in Fig. 21). Each figure showcases the complete pipeline from radiance field projections and complex 3D hologram rendering to both simulated and experimentally captured results, demonstrating consistent quality across different scene types and lighting conditions.

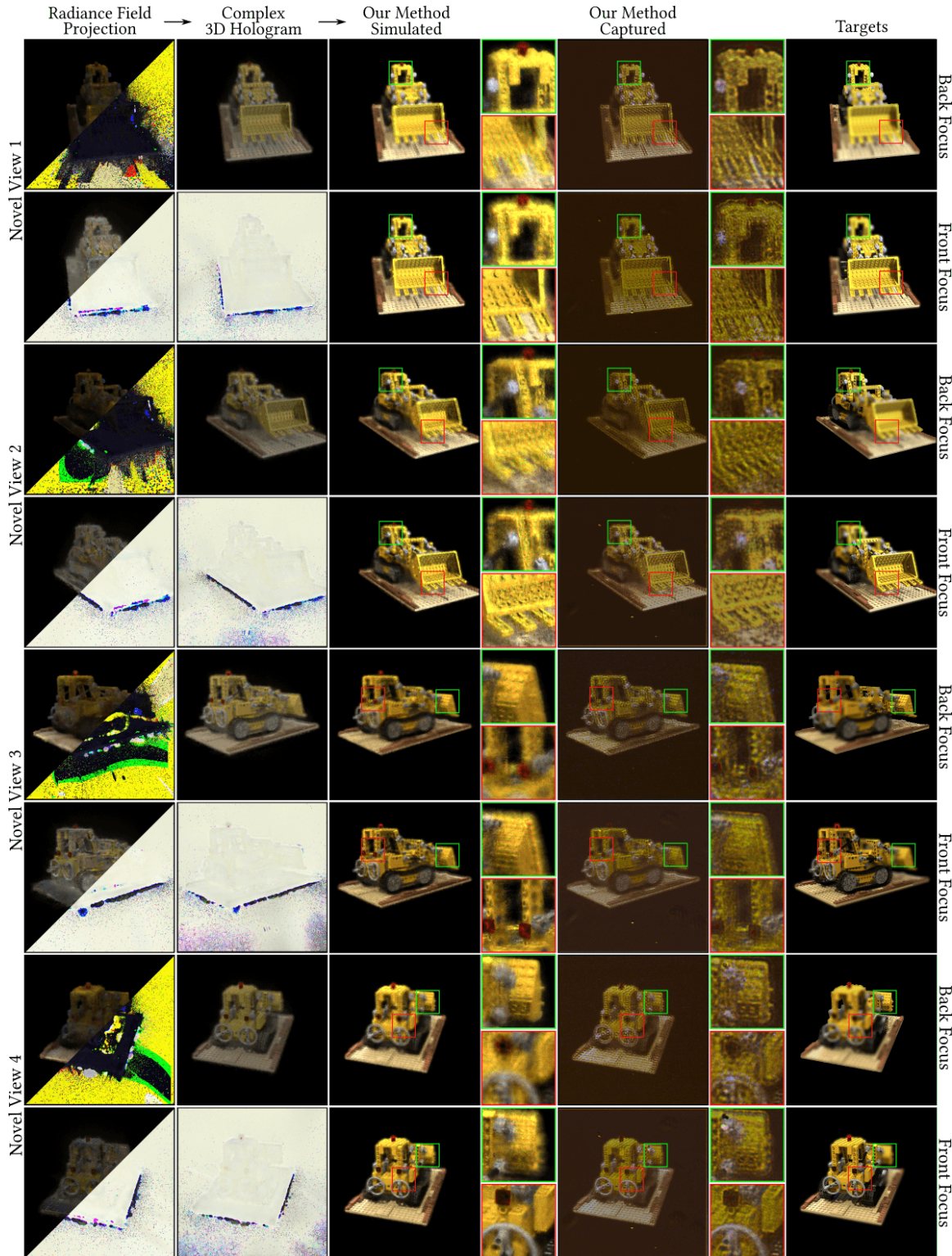


Fig. 13. Extra novel-view comparison of our method on lego scene from the NeRF Synthetic dataset. The first two columns show the radiance field projections and their rendered complex 3D holograms. The central columns present our method’s simulated results and experimentally captured results. The rightmost column displays the target images used as optimization objectives in our method.

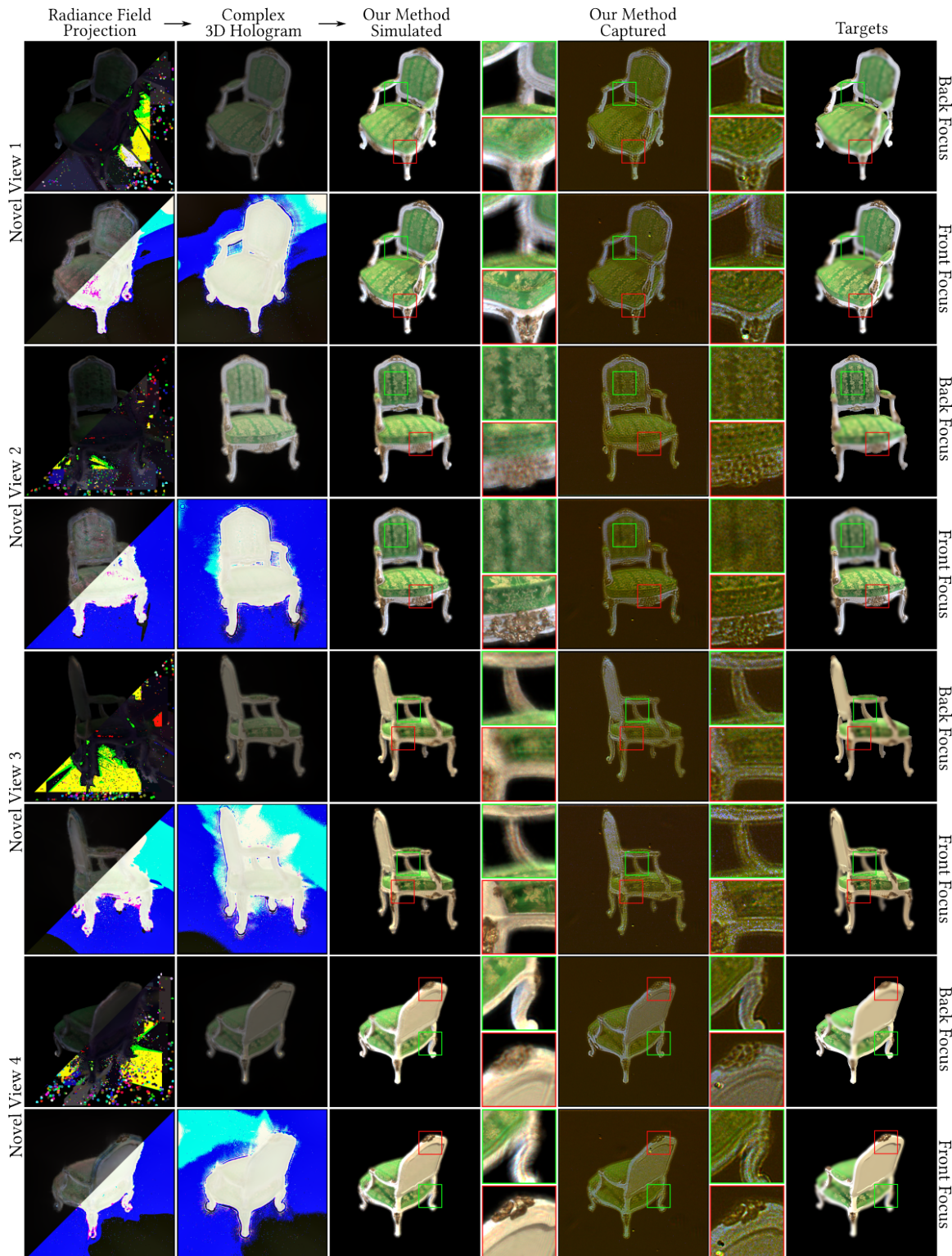


Fig. 14. Extra novel-view comparison of our method on chair scene from the NeRF Synthetic dataset. The first two columns show the radiance field projections and their rendered complex 3D holograms. The central columns present our method's simulated results and experimentally captured results. The rightmost column displays the target images used as optimization objectives in our method.

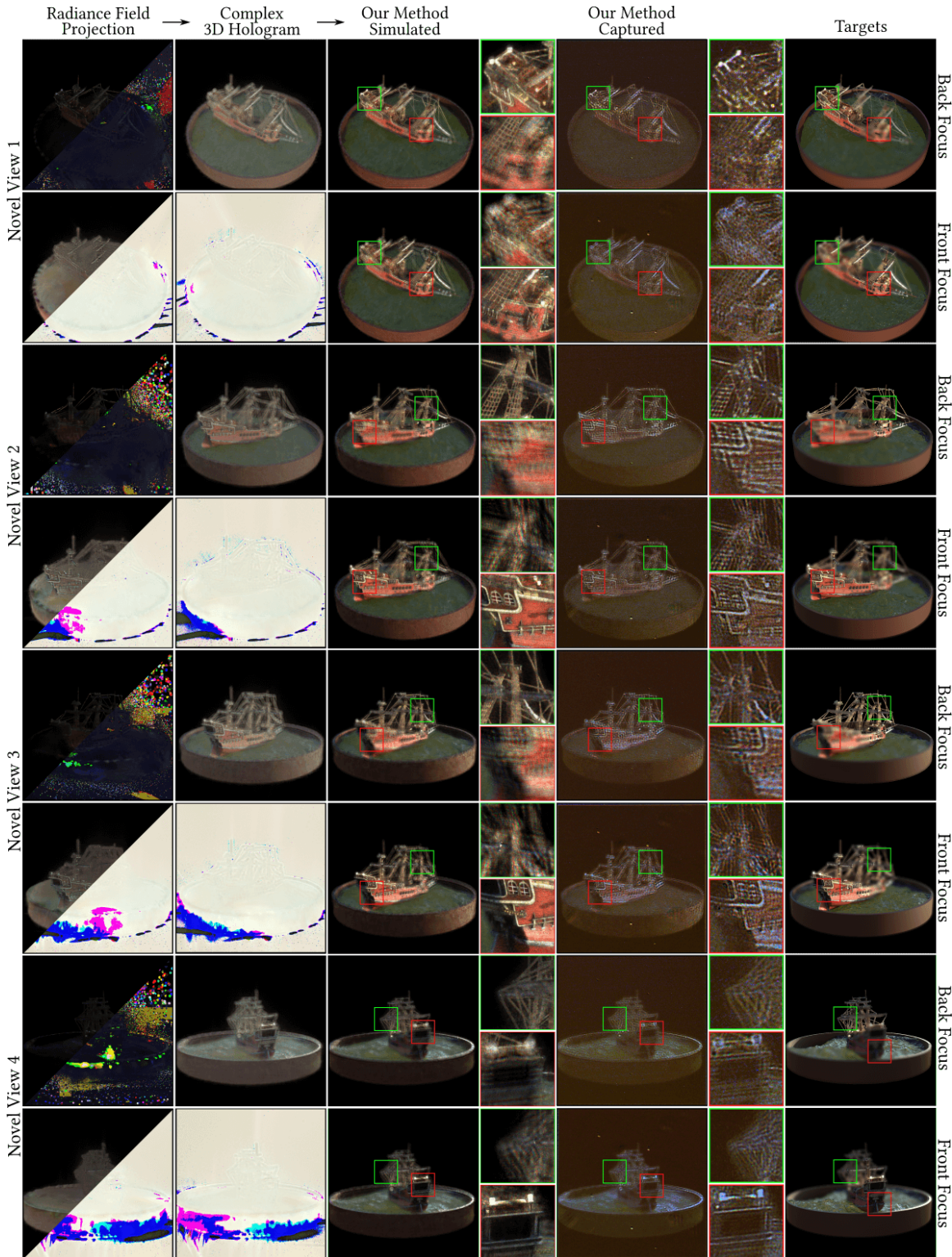


Fig. 15. Extra novel-view comparison of our method on ship scene from the NeRF Synthetic dataset. The first two columns show the radiance field projections and their rendered complex 3D holograms. The central columns present our method's simulated results and experimentally captured results. The rightmost column displays the target images used as optimization objectives in our method.



Fig. 16. Extra novel-view comparison of our method on materials scene from the NeRF Synthetic dataset. The first two columns show the radiance field projections and their rendered complex 3D holograms. The central columns present our method's simulated results and experimentally captured results. The rightmost column displays the target images used as optimization objectives in our method.



Fig. 17. Extra novel-view comparison of our method on hotdog scene from the NeRF Synthetic dataset. The first two columns show the radiance field projections and their rendered complex 3D holograms. The central columns present our method’s simulated results and experimentally captured results. The rightmost column displays the target images used as optimization objectives in our method.

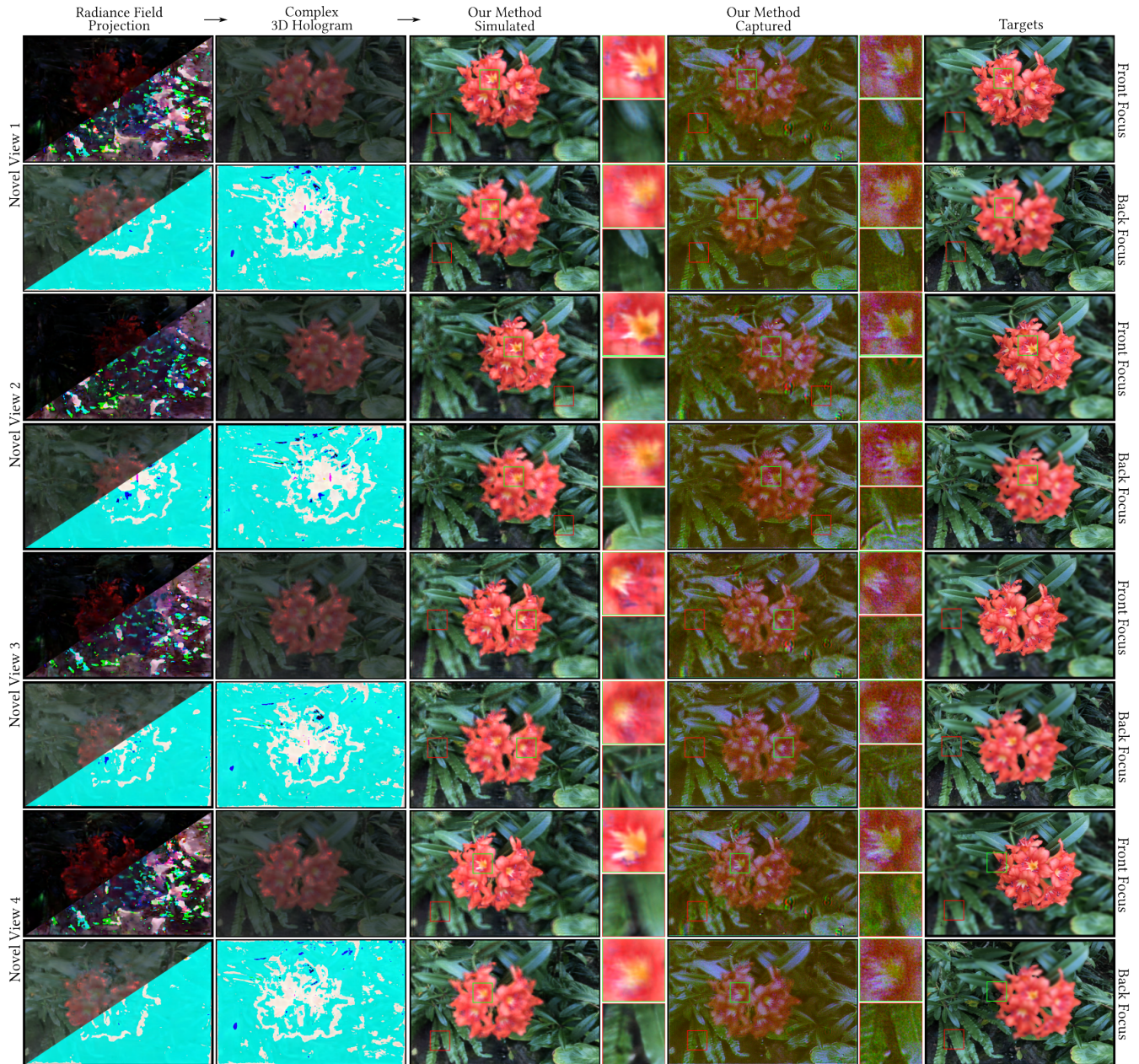


Fig. 18. Extra novel-view comparison of our method on flower scene from the LLFF dataset. The first two columns show the radiance field projections and their rendered complex 3D holograms. The central columns present our method’s simulated results and experimentally captured results. The rightmost column displays the target images used as optimization objectives in our method.



Fig. 19. Extra novel-view comparison of our method on fern scene from the LLFF dataset. The first two columns show the radiance field projections and their rendered complex 3D holograms. The central columns present our method’s simulated results and experimentally captured results. The rightmost column displays the target images used as optimization objectives in our method.



Fig. 20. Extra novel-view comparison of our method on trex scene from the LLFF dataset. The first two columns show the radiance field projections and their rendered complex 3D holograms. The central columns present our method's simulated results and experimentally captured results. The rightmost column displays the target images used as optimization objectives in our method.

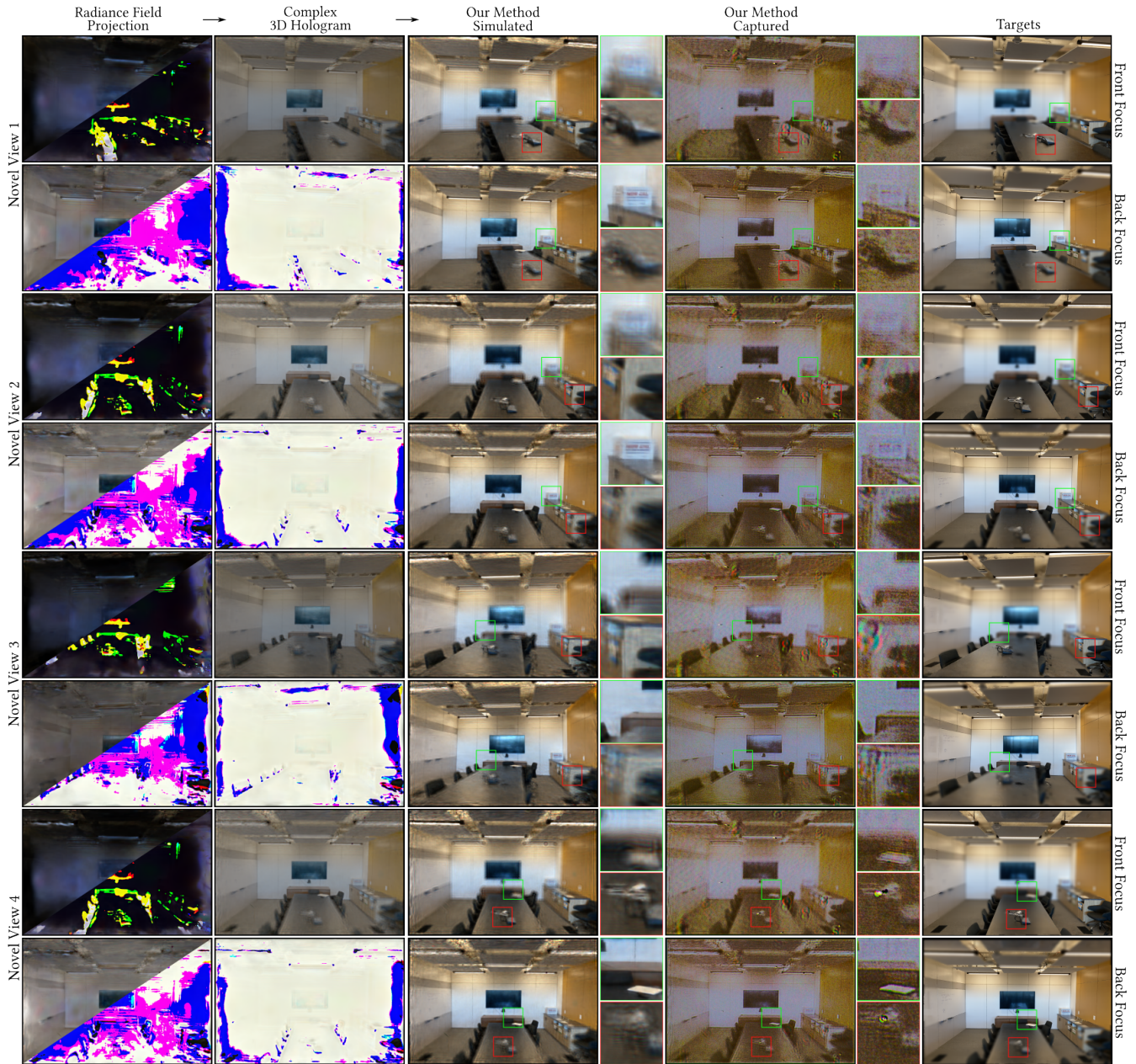


Fig. 21. Extra novel-view comparison of our method on room scene from the LLFF dataset. The first two columns show the radiance field projections and their rendered complex 3D holograms. The central columns present our method’s simulated results and experimentally captured results. The rightmost column displays the target images used as optimization objectives in our method.